Cell Stem Cell

Sphingolipid Modulation Activates Proteostasis Programs To Govern Human Hematopoietic Stem Cell Self-renewal

--Manuscript Draft--

Manuscript Number:	CELL-STEM-CELL-D-19-00044R3
Full Title:	Sphingolipid Modulation Activates Proteostasis Programs To Govern Human Hematopoietic Stem Cell Self-renewal
Article Type:	Research Article
Keywords:	Hematopoietic Stem Cells; umbilical cord blood; autophagy; unfolded protein response; sphingolipid metabolism; fenretinide; DEGS1; endoplasmic reticulum stress; UM171; StemRegenin-1
Corresponding Author:	John Dick University Health Network Toronto, ON CANADA
First Author:	Stephanie Z. Xie
Order of Authors:	Stephanie Z. Xie
	Laura Garcia-Prat
	Veronique Voisin
	Robin Ferrari
	Olga Gan
	Elvin Wagenblast
	Kerstin B Kaufmann
	Andy G.X. Zeng
	Shin-ichiro Takayanagi
	Ishita Patel
	Esther Lee
	Joseph Jargstorf
	Gareth Holmes
	Guy Romm
	Kristele Pan
	Michelle Shoong
	Aditi Vedi
	Chiara Luberto
	Mark D. Minden
	Gary D. Bader
	Elisa Laurenti
	John E. Dick
Abstract:	Cellular stress responses serve as crucial decision points balancing persistence or culling of hematopoietic stem cells (HSCs) for lifelong blood production. While strong stressors cull HSCs, the linkage between stress programs and self-renewal properties that underlie human HSC maintenance remains unknown, particularly at quiescence exit when HSCs must also dynamically shift metabolic state. Here, we demonstrate distinct wiring of the sphingolipidome across the human hematopoietic hierarchy and find that genetic or pharmacologic modulation of the sphingolipid enzyme DEGS1

	regulates lineage differentiation. Inhibition of DEGS1 in hematopoietic stem and progenitor cells during the transition from quiescence to cellular activation with N -(4-hydroxyphenyl) retinamide activates coordinated stress pathways that coalesce on endoplasmic reticulum stress and autophagy programs to maintain immunophenotypic and functional HSCs. Thus, our work identifies a linkage between sphingolipid metabolism, proteostatic quality control systems and HSC self-renewal and provides therapeutic targets for improving HSC-based cellular therapeutics.

Sphingolipid Modulation Activates Proteostasis Programs To Govern Human Hematopoietic Stem Cell Self-renewal

Stephanie Z. Xie[1,*], Laura Garcia-Prat[1], Veronique Voisin[2], Robin Ferrari[1], Olga I. Gan[1], Elvin Wagenblast[1], Kerstin B. Kaufmann[1], Andy G.X. Zeng[1,3], Shin-ichiro Takayanagi[1,4], Ishita Patel[1], Esther K. Lee[1], Joseph Jargstorf[1], Gareth Holmes[1], Guy Romm[1], Kristele Pan[1], Michelle Shoong[1], Aditi Vedi[5], Chiara Luberto[6], Mark D. Minden[1,7,8,9], Gary D. Bader[2,3], Elisa Laurenti[5], and John E. Dick[1,3,10,*]

[1]Princess Margaret Cancer Centre, University Health Network, Toronto, Ontario, M5G0A3, Canada
[2]The Donnelly Centre, University of Toronto, Toronto, Ontario, M5S3E1, Canada
[3]Department of Molecular Genetics, University of Toronto, Toronto, Ontario, M5S1A8, Canada
[4]R&D Division, Kyowa Kirin Co., Ltd., Tokyo, 194-8533, Japan
[5]Wellcome-Medical Research Council Cambridge Stem Cell Institute, Department of Haematology, University of Cambridge, Cambridge, United Kingdom
[6]Department of Physiology and Biophysics, Stony Brook School of Medicine, Stony Brook, 11794, USA
[7]Division of Medical Oncology and Hematology, Department of Medicine, University Health Network, Toronto, Ontario, Canada
[8]Department of Medicine, University of Toronto, Toronto, Ontario, Canada
[9]Department of Medical Biophysics, University of Toronto, Toronto, Ontario, Canada
[10]Lead Contact

[*] Correspondence: sxie@uhnresearch.ca (S.Z.X.), jdick@uhnresearch.ca (J.E.D.)

Summary

Cellular stress responses serve as crucial decision points balancing persistence or culling of hematopoietic stem cells (HSCs) for lifelong blood production. While strong stressors cull HSCs, the linkage between stress programs and self-renewal properties that underlie human HSC maintenance remains unknown, particularly at quiescence exit when HSCs must also dynamically shift metabolic state. Here, we demonstrate distinct wiring of the sphingolipidome across the human hematopoietic hierarchy and find that genetic or pharmacologic modulation of the sphingolipid enzyme DEGS1 regulates lineage differentiation. Inhibition of DEGS1 in hematopoietic stem and progenitor cells during the transition from quiescence to cellular activation with *N*-(4-hydroxyphenyl) retinamide activates coordinated stress pathways that coalesce on endoplasmic reticulum stress and autophagy programs to maintain immunophenotypic and functional HSCs. Thus, our work identifies a linkage between sphingolipid metabolism, proteostatic quality control systems and HSC self-renewal and provides therapeutic targets for improving HSC-based cellular therapeutics.

Introduction

Humans have an enormous demand (~10^{e12} cells daily) for hematopoietic output. Meeting this need over a lifetime raises an inherent risk for malignancy due to DNA replication errors and potential metabolic and cellular stressors that cause cellular damage (Doulatov et al., 2012; Kohli and Passegue, 2014). Yet hematologic malignancies remain relatively rare. The hierarchical organization of blood is thought to mitigate the risk of transformation. All mature lineages descend from a pool of rare and largely quiescent long-term hematopoietic stem cells (LT-HSC) that in turn generate highly proliferative but more short-lived populations including short-term HSC (ST-HSC) and committed progenitors. Only LT-HSC are able to regenerate the entire blood system upon transplantation and maintain long-term output due to their unique capacity for self-renewal. Whereas dormancy in LT-HSC minimizes the possibility of detrimental mutations passing to all progeny, damage arising within the rapidly proliferating downstream progenitors are ultimately purged upon terminal differentiation (Milyavsky et al., 2010; Mohrin et al., 2010). However, recent studies have found that dormancy is not the only feature that uniquely protects LT-HSC. Compared to downstream progenitors, stressed or damaged LT-HSC respond by activating pathways that result in culling rather than pathways that serve to repair or resolve the damage as is typical for progenitors and most mammalian cell types (Milyavsky et al., 2010; Mohrin et al., 2010). How this unique LT-HSC fate choice is made is poorly understood, particularly upon quiescence exit when LT-HSC must also dynamically shift metabolic state. The unfolded protein response (UPR) and macroautophagy, hereafter referred to as autophagy, have been identified as critical mediators for HSC stress responses (Ho et al., 2017; van Galen et al., 2014; Warr et al., 2013). More broadly, these new findings revealed an unexplored layer of metabolic and organelle biology that influences LT-HSC regulation of self-renewal, quiescence, proliferation and lineage commitment that extends beyond the traditional focus on transcription factor networks governing fate decisions (Wilkinson and Göttgens, 2013).

The energy and macromolecule requirements of HSC are distinct from progenitors and genetic ablation of key metabolic regulators in mouse models often lead to HSC exhaustion; as such, stringent control of cellular metabolism is fundamental for HSC function (Gan et al., 2010; Gurumurthy et al., 2010; Ito and Suda, 2014; Nakada et al., 2010; Simsek et al., 2010; Takubo et al., 2013; Wang et al., 2014). Recent data suggest that HSC contain integrated cellular networks coordinating proteostasis with dynamic biosynthetic and metabolic states to govern stem cell fate decisions especially in the transition from dormancy to cellular activation (Gurumurthy et al., 2010; Mohrin et al., 2015; Warr et al., 2013). Presumably, quality control mechanisms ensure HSC organelle and proteostatic health upon damage incurred from cell cycle entry and other basal metabolic stressors such as reactive oxygen species (ROS) (Garcia-Prat et al., 2017). However, metabolic as well as translation initiation heterogeneity cannot be attributed entirely to cellular identity differences between LT-HSC and committed progenitors; dormant HSC exhibit lower biosynthetic activity and protein synthesis than active HSC, suggesting HSC metabolic requirements are highly adaptive to cellular state (Cabezas-Wallscheid et al., 2017; Signer et al., 2014). Additionally, the dysregulation of quality control mechanisms (e.g. autophagy) that occur upon HSC aging results in metabolic changes, suggesting that HSC fate is intimately entangled with metabolic and proteostatic regulation (Ho et al., 2017; Kohli and Passegue, 2014). Enhanced

endoplasmic reticulum (ER) function in human HSC with enforced expression of the chaperone ERDJ4/DNAJB9 confers protection against the ER stress that is induced upon xenotransplantation thereby preserving self-renewing HSC (van Galen et al., 2014). Moreover, we recently showed higher levels of activating transcription factor 4 (ATF4) and components of the pro-survival integrated stress response (ISR) in human HSC are cytoprotective during homeostasis despite their lowered threshold for culling with strong stress stimuli (van Galen et al., 2018). Thus, a complex picture emerges suggesting the nature of the stress stimulus is important to fine-tune quality control responses for HSC persistence or culling. However, these studies raise a number of key questions: is there a single stimulus that activates both autophagy and the UPR to confer cytoprotective functions to HSC; is there a coordinated cellular stress response upon stress induction; and how do proteostasis programs impact HSC self-renewal?

Proper management of lipid composition is integral for maintaining cellular membrane dynamics for cell division and signaling in cell lines (Atilla-Gokcumen et al., 2014; Koberlin et al., 2015). Although lipid homeostasis is critical for cellular and organismal health, the exploration of lipid metabolism in HSC function is limited (Hotamisligil, 2017; Ito et al., 2012; Ito et al., 2016). While lipostatic stress as well as proteostatic stress is known to converge on the activation of the UPR for pro-survival in human cells, and autophagy is a crucial element for maintaining lipid homeostasis in mice (Singh et al., 2009; Thibault et al., 2012), there is a critical lack of understanding on the impact of altering lipid composition to HSC function beyond the connection of fatty acid metabolism and mitochondrial function (Ito et al., 2016). Ceramide (Cer), the central component of sphingolipids (SpLs), has been proposed to be part of a lipid biostat that regulates cellular stress and activates stress responses (Hannun, 1996; Hannun and Obeid, 2018). DEGS1 (Delta 4-Desaturase, Sphingolipid 1, or DES1) is an ER membrane spanning protein and the final enzyme in *de novo* SpL synthesis, which converts dihydroceramide (dhCer) to Cer; both genetic ablation and inhibition with the synthetic retinoid fenretinide/*N*-(4-hydroxyphenyl) retinamide (4HPR) is sufficient to activate autophagy in mouse cells or human cell lines (Siddique et al., 2015; Siddique et al., 2013). The potent bioactive lipid sphingosine-1-phosphate (S1P) is generated from metabolism of Cer and exerts pleiotrophic signaling roles in proliferation, survival, migration of immune cells and HSC, as well as regulation of lymphocyte lineage commitment and hematopoietic stem and progenitor (HSPC) function (Blaho et al., 2015; Golan et al., 2012; Juarez et al., 2012; Massberg et al., 2007; Schwab et al., 2005). Although S1P signaling regulates mouse hematopoiesis, whether other SpLs are important to HSC function is unknown.

Here, we uncovered a transcriptional signature of genes governing SpL synthesis that distinguishes human HSC and committed progenitors. This distinct SpL wiring in the human hematopoietic hierarchy was confirmed with sphingolipidomic analysis of sorted mature and HSPC populations. When human HSC are placed in *ex vivo* conditions thought to promote cord blood (CB) HSC activation and expansion, they actually lose HSC function due to impaired proteostatic programs. By contrast, inhibition of DEGS1 in human HSC with 4HPR treatment before quiescence exit in *ex vivo* culture induced a coordinated response of proteostatic cellular stress programs including autophagy to maintain HSC self-renewal. Despite *ex vivo* culture, HSC following SpL modulation functionally show higher self-renewal relative to cultured cells without treatment pointing to a linkage between SpLs, proteostatic quality control programs, and HSC

self-renewal in the transition from quiescence to cellular activation.

Results

DEGS1 influences SpL composition in the human hematopoietic hierarchy and is functionally required for HSC repopulation

We undertook transcriptome analysis of highly resolved subpopulations of the human hematopoietic hierarchy and found that lipid signaling and metabolism genes involved in SpLs are differentially expressed (FDR<0.05, FC>1.5) in LT-HSC and ST-HSC (as defined in (Laurenti et al., 2015; Notta et al., 2011; Notta et al., 2016)) compared to committed progenitors (Figure 1A and S1A). Previous lipid measurements of mammalian cells indicated that SpLs contribute only ~10% of the cellular lipidome, mostly represented by structural sphingomyelins (SM) and glycosphingolipids (van Meer and de Kroon, 2011). Overlaying the differentially expressed SpL genes (Figure 1A) onto the metabolic pathway (Hannun and Obeid, 2018) showed many of the SpL genes highly expressed in HSC centred around those involved in the synthesis of the low abundant bioactive dhCer and Cer species (Figure S1A). To assess whether there is distinct SpL biosynthesis across the cell types comprising the human hematopoietic hierarchy, especially at the level of these less abundant SpLs, we isolated $CD34^+CD38^-$ stem-enriched (stem) and $CD34^+CD38^+$ progenitor-enriched (progenitor) cells and 5 mature blood lineages (B and T lymphocytes, monocytes, neutrophils and erythrocytes) from CB by flow cytometry. These populations were subjected to Cer, dhCer, sphingosine, S1P, dhSph, dhS1P, hexosylceramides (HexCer, Cer containing glucose or galactose) and SM measurement using liquid chromatography mass spectrometry (LC-MS) (Figure 1B, S1B-H). SM were the most abundant SpLs in our analysis (Figure 1B, S1H, 72%-94%), consistent with previous lipidome profiling in mammalian cells (van Meer and de Kroon, 2011). Importantly, our profiling identified the accumulation of S1P specifically in erythrocytes (Figure S1E) confirming this lineage-specific association and the robustness of our sphingolipidome profiling (Dahm et al., 2006). We found no significant differences in SpL content between stem and progenitor cells except in the amount of dhCer carrying the C16:0 fatty acid providing evidence for differential wiring of *de novo* SpL synthesis at the lipid level in HSPC (Figure 1C). By contrast, the mature lineages showed significant differences from stem and/or progenitor cells (Figure S1C-H). Importantly, we saw that B cells, neutrophils and erythrocytes were significantly different in their ratio of Cer/dhCer from stem cells (Figure 1D). In contrast, T cells and monocytes did not differ in the Cer/dhCer ratio raising the question of whether Cer homeostasis regulates HPSC fate and lineage commitment decisions. DEGS1 expression levels are significantly increased in LT-HSC, ST-HSC and granulocyte-monocyte progenitors (GMP) following 6 hours of cytokine stimulation, suggesting increasing *de novo* SpL generated Cer pools may be an early event in the transition from quiescence to cellular activation (Figure 1E). To determine whether alterations in the Cer/dhCer ratio were functionally relevant in HSPC, we modulated their ratio through DEGS1 perturbation and asked if DEGS1 was required for *in vivo* repopulation. A lentiviral knockdown (KD) construct to DEGS1 was generated that decreased DEGS1 gene expression to 37% of shCtrl in a cell line model (Figure S1I). CB stem cells were transduced *in vitro* with either shCtrl or shDEGS1 vectors co-expressing BFP and transplanted into mice. At 4 weeks, we found DEGS1 KD significantly decreased human $CD45^+$

BFP^+ chimerism by 2-fold relative to BFP^+ input and resulted in lineage skewing with an increase in myeloid cells at the expense of B lymphoid cells (Figure 1F, G, S1J-O). In summary, we have uncovered considerable diversity in SpL composition across the human hematopoietic hierarchy and found that human HSPC require DEGS1 *in vivo*.

Sphingolipid modulation with the DEGS1 inhibitor 4HPR alters HSC function and lineage balance *in vitro*

To determine whether DEGS1 is required as part of the proper transition from quiescence to cellular activation and/or self-renewal maintenance in human HSC, its function must be inhibited at the start of quiescence exit. As lentiviral transduction of $CD34^+$ cells requires some period of cytokine pre-stimulation to induce cellular activation (Amirache et al., 2014), we used the irreversible DEGS1 inhibitor 4HPR at 2 μM (Rahmaniyan et al., 2011; Siddique et al., 2015) at the start of cytokine activation. This dose caused 50% maximal reduction in total cells of lineage-depleted CB (lin-CB) cells after 3 days in culture (Figure S2A). 4HPR treatment for 8 days altered SpL composition resulting in decreased Cer and increased dhCer compared to controls (Figure 2A, S2B, and S4A-D). BrdU incorporation in LT-HSC, ST-HSC, and GMP was decreased by 4HPR treatment at day 3 suggesting modulating Spls in HSPC decreases proliferation in *vitro* (Figure S2C). Nonetheless, 4HPR treatment still permits quiescence exit and does not significantly alter cell viability (Figure S2D-E). Similarly, there was no difference in cell cycle distribution between shCtrl and shDEGS1 in LT-HSC or in GMP isolated from mice at 4 weeks transplantation suggesting DEGS1 KD does not lock cells into quiescence *in vivo* (Figure S2F). Next, we utilized the colony forming cell assay (CFC) to assess *in vitro* progenitor function to determine if DEGS1 inhibition alters functional output from HSPC subpopulations. 4HPR treatment significantly increased clonogenic output specifically from LT-HSC (50% over control), but not from ST-HSC or GMP (Figure 2B). Treatment of LT-HSC and ST-HSC with 4HPR led to an increased proportion of granulocyte-macrophage (GM) and M colonies (Figure 2C). Flow cytometry confirmed the morphologic CFC assessment that 4HPR enhanced myeloid output at the expense of erythroid (Figure 2D-E). As 4HPR resembles all-trans retinoic acid (ATRA) and may have additional effects independent of DEGS1, CFC assays were performed on LT-HSC, ST-HSC, and GMP treated with ATRA but did not mimic 4HPR treatment (Figure S2G). Whilst 4HPR effects appeared independent of the retinoid pathway, other potential off-target effects on HSC function were possible. Thus, we turned to a genetic approach with DEGS1 KD and transduced LT-HSC, ST-HSC and GMP with shCtrl or shDEGS1 vectors and sorted BFP^+ transduced cells for CFC assays. We found that shDEGS1 LT-HSC showed similar, but more modest changes in colony distribution and loss of erythroid output (Figure 2F-G). The more modest effects of DEGS1 KD may be reflective of the more modest, but measurable changes in Cer and dhCer levels compared to control KD in cells isolated from xenografts (Figure 2H-I, S2H). Thus, DEGS1 modulation pharmacologically or via KD alters lineage balance *in vitro* and 4HPR modulation of SpL homeostasis selectively enhances clonogenic efficiency only in LT-HSC.

***Ex vivo* treatment with 4HPR maintains HSC function following xenotransplantation**

To directly test whether 4HPR modulation of SpL impacts LT-HSC function, we utilized the xenograft assay to selectively read out self-renewal capacity from culture-generated progeny with HSC function. Our approach to test 4HPR was guided by *ex vivo* expansion methods (Kiernan et al., 2016) that are used clinically to expand CB derived HSPC, as single CB units do not contain enough HSC to enable HSC transplantation (HSCT) into adult recipients in the clinic. Thus, we added 4HPR into an expansion scheme with lin^- CB cells containing LT-HSC, ST-HSC and committed progenitors that was similar to recently developed state of the art methods for CB transplantation (Fares, et al., 2014). Three initial cell concentrations corresponding to high (16), medium (3.2), and limiting (0.65) long-term repopulating cells (LTRC) doses were cultured *ex vivo* for 8 days mimicking fed-batch conditions (Csaszar et al., 2012), and then their progeny were analyzed by flow cytometry and assessed for engraftment potential by xenotransplantation (Figure 3A, see methods). 4HPR-treated cultures had fewer $CD34^+$ cells, enhanced myeloid differentiation and decreased erythroid differentiation (Figure 3B-F). Despite fewer $CD34^+$ cells at transplantation, human CD45 chimerism for control and 4HPR treated progeny were similar in all cell doses following xenotransplantation (Figure 3G). Similarly, lineage distribution for B lymphoid, myeloid, and erythroid lineages (Figure 3H-J) and the percentage of lin^- CD34+ cells (Figure 3K) from the 16 LTRC dose was comparable for control and 4HPR treated groups. Flow cytometry analysis of the HSC hierarchy in individual mice confirmed all HSPC subpopulations analyzed exhibited similar experimental variation between mice transplanted with control and 4HPR treated cells (Figure S3A-I). These data indicate that despite reduced $CD34^+$ cell output, the quality and quantity of functionally defined repopulating HSC from 4HPR cultured cells at 16 weeks xenotransplantion was similar to controls where far higher numbers of CD34+ cells were transplanted. Moreover, lineage differentiation effects resulting from *ex vivo* modulation of SpLs in HPSC by 4HPR are transient and reversible following xenotransplantation since the number of HSPC regenerated in the mice was equivalent to controls. In contrast, when DEGS1 is genetically modulated via KD, we observed a severe decrease (4.5-fold decrease over shCtrl, Figure S3J) in the number of $CD34^+$ at 4 weeks *in vivo*. Hence, reducing DEGS1 activity transiently or persistently restrains the generation of $CD34^+$ progeny.

Sphingolipid modulation restricts expansion of committed progenitors during *ex vivo* culture to enhance HSC self-renewal

To determine if 4HPR treatment caused a potential dissociation between phenotypic and functional HSPC during culture, we quantitatively assess the HSC self-renewal capacity of 4HPR treated CB progeny using serial transplantation approaches. In contrast to previous strategies which focused on the expansion of $CD34^+$ cells to improve the clinical utility of CB as a HSCT source, SpL modulation by 4HPR here restrained proliferation and resulted in 3.3-fold fewer $CD34^+$ cells relative to control treatment (Figure 3F). Therefore, we investigated in parallel the effects of two known CB $CD34^+$ agonists UM171 and SR1 (Boitano et al., 2010; Fares et al., 2014) alone and in combination with 4HPR. First, we assessed the clonogenic activity of LT-HSC in CFC assays and found that 4HPR significantly increased clonogenic activity in combination with either UM171 or SR1 to levels similar to 4HPR alone (Figure 4A). In contrast, UM171 or SR1 alone did not increase clonogenic activity of LT-HSC. Next, we cultured 2 independent pools of lin^-CB with DMSO control, 4HPR, UM171+SR1 (U+S) and UM171+SR1+4HPR (3-Factor) for 8 days and found

4HPR treatment restricted the percentage and number of $CD34^+$ cells, while 3-Factor treatment resulted in an enhanced percentage of CD34+ cells comparable to U+S treatment (Figure 4B). The total number of cells following 8 days culture was similar between 4HPR and 3-Factor treatment (Figure S4A). We performed LC-MS analysis and found the SpLs measured in 3-Factor progeny phenocopied 4HPR treatment and were similarly perturbed (Figure S4B-D). We further analyzed $CD34^+$ cells at day 8 culture for cultured LT-HSC (cLT:CD90+CD45RA-), ST-HSC (cST:CD90-CD45RA) and cultured committed progenitors (cProg:CD90-CD45RA+) (Figure 4C). 4HPR alone significantly limited the percentage of cProg cells while increasing cST cells in the CD34 compartment and trended to increased cLT cells relative to control; 3-Factor treatment resulted in significant enrichment of both cLT and cST populations (Figure 4C-D). The functional identity of these subpopulations was confirmed in an independent experiment by xenotransplantation for 16 weeks; as expected cProg cells were unable to give rise to human CD45 grafts (Figure S4E-G). Hence, these data show 4HPR acts dominantly over UM171 or SR1 to enhance LT-HSC clonogenic ability and 3-Factor treatment during *ex vivo* culture increases immunophenotypic HSC subsets.

To determine if 4HPR alone or 3-Factor enhances *in vivo* HSC self-renewal following *ex vivo* treatment, lin^- CB progeny cultured with control, 4HPR, U+S or 3-Factor for 8 days were serially transplanted into NSG mice (Figure 3G, S4H). In line with previous work on UM171 and SR1, U+S or 3-Factor *ex vivo* treatment significantly increased primary engraftment of CB cells (Figure S4H; Fares et al., 2014). Next, human $CD45^+$ cells engrafted at 16 LTRC doses were serially transplanted in a limiting dilution assay (LDA) to enumerate functional LTRC from the primary recipients for 5 independent pools of CB treated with 4HPR; the total period of engraftment was 32 weeks. 4HPR-treated cells showed a significant 2.5-fold increase in LTRC frequency over control upon secondary transplantation (Figure 4E-F, p=0.039). In the 2 experiments where U+S were also assessed, 4HPR alone resulted in 2.1-fold increase in LTRC frequency, similar to the frequency obtained by combining the five experiments (Figure 4E-F; S4I-J). However, the LTRC frequency of U+S treated cells was similar to control. Importantly, 3-Factor-treated cells gave a 4.7-fold augmentation in LTRC frequency over cultured control cells (p=0.007). Collectively, these transplantation data showed that CB expansion with 4HPR alone and in combination with U+S successfully sustained a pool of functional HSC during *ex vivo* culture with enhanced *in vivo* HSC self-renewal capacity relative to controls.

4HPR activates a coordinated cellular stress response including autophagy and the UPR/ISR during *ex vivo* culture

To elucidate the biological pathways altered by 4HPR treatment in human HSPC that contributed to lineage differentiation effects and maintenance of HSC self-renewal during cytokine activation, we performed RNA-sequencing (RNA-Seq) on lin^- CB cells at days 2 and 4 following treatment with control, 4HPR, U+S, and 3-Factor (n=3). GSEA Pathway analysis identified 473 significantly upregulated gene sets and 80 significantly downregulated gene sets (FDR<0.05) in 4HPR compared to controls at day 2 (Figure S5A, Table S1). Many of the upregulated pathways following 4HPR treatment centered around cell cycle progression which is consistent with the decreased S phase progression in HSPC subsets we observed following 4HPR treatment (Table S1; Figure S2C). Lipid metabolism pathways were significantly altered with an upregulation of

Cer/SpL biosynthesis and a decrease in cholesterol/sterol biosynthetic pathways (Figure 5A); possibly a feedback response due to SpL homeostasis disruption by 4HPR (Koberlin et al., 2015; Singh et al., 2009). Interestingly, a strong cellular stress induction theme was highlighted in the pathway analysis (FDR<0.05, Figure S5A) following 4HPR treatment, including ER stress/UPR/ATF4, protein folding, ROS and autophagy. These pathways were grouped into 6 modules and GSEA showed a significant enrichment of these pathways for 4HPR treatment relative to control (Figures 5A-B, shaded gray on S5A, gene lists in Table S2).

We asked if some of these stress response programs following 4HPR-induced lipostatic stress are potentially intrinsic HSC maintenance mechanisms necessary for cellular activation. When we analyzed ER stress/UPR, protein folding, ROS and autophagy in uncultured LT-HSC compared to uncultured GMP by GSEA, only autophagy was not significantly enriched, suggesting some stress response programs are more activated in progenitors than HSC at homeostasis (Figure S5B). To distinguish cell cycle priming as opposed to lineage priming differences between LT-HSC and GMP, we compared ST-HSC to LT-HSC at homeostasis and we found a significant enrichment of protein folding (p=0.001) and near significant enrichment of ER stress/UPR (p=0.079) in LT-HSC suggesting these programs may be required for quiescence exit and/or self-renewal (Figure 5C). Additionally, we analyzed published single cell RNAseq data of HSC from bone marrow (Velten et al., 2017). Within $CD34^{+}CD38^{-}CD45RA^{-}$ cells, we identified two clusters, cell cycle-primed and non-primed, using a clustering algorithm developed to robustly find distinguishing gene expression features in stem cells (Tarashansky et al., 2018, see methods). We specifically examined LT-HSC, which were represented in both clusters, and found that cell cycle-primed LT-HSC have higher CD38 surface expression, cell cycle programs, and CDK6 and DEGS1 expression than non-primed LT-HSC (Figure S5C-D, 5D-E). The latter had enrichment for a set of dormancy-associated genes found in label-retaining dormant mouse LT-HSC (Figure S5E, Cabezas-Wallsheild, et al., 2017). We found ER stress/UPR and protein folding enriched in cell cycle-primed LT-HSC suggesting the activation of ER proteostasis programs as well as upregulation of DEGS1 gene expression is an early event in HSC activation.

Next, we asked how the gene expression changes enacted by 4HPR treatment compared to combination treatment with U+S during culture and changed over time. Cells subjected to 3-Factor treatment at day 2 showed negative enrichment for cholesterol/sterol biosynthesis pathways and at day 4 also showed enrichment of ER stress and UPR pathways as observed with 4HPR alone (Table S1). Gene expression changes for the top 4 genes in the selected pathways are similar following 4HPR treatment and 3-Factor treatment, but 3-Factor treated samples show fewer significantly altered gene sets than with 4HPR treatment alone at both days 2 and 4 (Figure 5F, Figure S5F-G). These data point to activation of autophagy and ROS gene sets as resulting exclusively from 4HPR treatment. While cytokine treatment induces cell cycle entry but no cell division in LT-HSC at day 2 (progenitors have divided), most LT-HSC have completed one cellular division only by day 4 (Figure S2D, (Laurenti et al., 2015). Nonetheless, gene expression changes in ER stress/UPR and metabolic gene sets persist from day 2 to day 4 (Table S1; Figure S5F-H) suggesting 4HPR treatment is provoking a sustained HSC maintenance response in *ex vivo* culture independently of cell cycle transit following quiescence exit.

We had previously identified a cytoprotective ATF4-ISR program downstream of the UPR in response to metabolic stress in human HSC (van Galen et al., 2018). Since we retrieved enrichment in the ER stress/UPR functional model for an "ATF4 activated genes" gene set by 4HPR treatment, we asked if HSC subsets following DEGS1 KD also showed evidence for activation of this UPR/ATF4 program. We quantified phosphorylated eukaryotic translation initiation factor 2α (eIF2α) in LT-HSC and ST-HSC from 4 week xenografts engrafted with shCtrl or shDEGS1 transduced HSPC by confocal microscopy (Figure 5G-H, 3 CB from experiment 2 of Figure S1J-M). Upon UPR activation by ER stress, eIF2α is phosphorylated to attenuate eIF2B resulting in global translation inhibition except for the specific transcriptional programs, e.g. ATF4, licensed by the UPR (Hetz et al., 2013). As LT-HSC are activated with 60% are cycling at 4 weeks transplant, the presence of anti-pEIF2S1/phospho-eIF2α staining in shCtrl LT-HSC and ST-HSC reflects activation of an UPR/ISR program (Figure 5G-H, S2F, S5I; Laurenti et al., 2015; van Galen et al., 2018). Importantly, shDEGS1 LT-HSC have significantly increased pEIF2S1 staining over shCtrl suggesting LT-HSC are more sensitive to lipostatic stress than ST-HSC *in vivo* (Figure 5G-H, S5J-K). Thus, these data suggest SpL modulation via pharmacological inhibition *ex vivo* and via lentiviral KD *in vivo* are activating an UPR/ATF4 program during cellular activation to restore homeostasis.

Metabolic dysregulation through increase in oxidative stress and mitochondrial dysfunction are known activation signals for ATF4-ISR programs (Kasai et al., 2019). Pathways related to redox homeostasis, mitochondria gene sets and Pink-Parkin mediate mitophagy suggest 4HPR treatment has activated the UPR/ATF4 to enact metabolic remodeling to restore homeostasis (Table S1). Therefore, we analyzed two metabolic parameters following 2 days of 4HPR treatment in the progeny of CB stem and progenitor cells (Figure 5I-J, S5L-M). Decreased ROS and mitochondrial membrane potential were observed following 4HPR treatment as compared to control in both populations. Such metabolic reprogramming by 4HPR persists to day 3 when the progeny of HSPC including LT-HSC treated with 4HPR have exited quiescence and are actively cycling (Figure S5L-M, S2D). In summary, as DEGS1 functions at the ER to convert dhCer to Cer, which is then further processed at the Golgi apparatus to form complex SpLs (Thibault et al., 2012; Zheng et al., 2006), these data are consistent with 4HPR inhibition of DEGS1 as a lipostatic stress stimulus capable of activating coordinated transcriptional stress programs to remodel the cellular metabolism of cultured HSPC for stress recovery and ultimately preserve functional HSC.

Sphingolipid modulation specifically activates autophagy in stem and not progenitor cells

As activating autophagy can promote HSC function (Chen et al., 2009; Luo et al., 2014), we asked if 4HPR treatment leads to autophagy activation for HSC maintenance during *ex vivo* culture. Gene expression analysis showed SpL modulation by 4HPR upregulated autophagy gene sets in lin^- CB. However, autophagy has not previously been characterized in human LT-HSC in quiescence or upon cellular activation. Thus, we examined basal autophagy in CB LT-HSC and GMP with the autophagosome marker LC3II by confocal microscopy and found similar LC3II intensity consistent with murine data (Figure 6A, S6A-B, (Ho et al., 2017)). To ascertain if *in vivo* cellular activation disrupts basal autophagy levels in human HSC, we compared LC3II staining in LT-HSC isolated from G-CSF mobilized peripheral blood (mPB) (Figure 6B, S6C) and found a significant decrease in LC3II intensity in mPB LT-HSC compared to CB LT-HSC. Next, we asked if

4HPR treatment specifically activated autophagy in human CB stem cells and not progenitors, since only murine stem cells appear capable of activating autophagic flux in response to metabolic stress (Warr et al., 2013), with two independent assays: 1) LC3II staining with and without bafilomycin A1 (BAF), an agent that inhibits autophagosome turnover by blocking lysosome acidification (Figure 6C-F, S6D-E) and 2) flow cytometry with Cyto-ID (Figure 6G-H, SG-I). LC3II staining showed both control and 4HPR-treated stem and progenitor cells at day 2 exhibit basal autophagy in culture (Figure 6D-E, S6D). However, only stem but not progenitor cells showed autophagy activation by an increase in LC3II foci area in the presence of 4HPR and BAF (Figure 6D-F). Similarly, Cyto-ID staining with control or 4HPR-treated cells (0.2 μM or 2 μM) showed that 4HPR significantly amplified autophagic flux only in stem but not in progenitor cells (Figure 6G). We confirmed cytokine withdrawal activates autophagy (as measured by Cyto-ID) in human stem but not progenitor cells like in mouse (Figure 6H, S6F-G), which is further enhanced by 4HPR (Figure 6SH). Collectively, these data indicate 4HPR activated autophagy exclusively in stem cells during *ex vivo* culture.

Sphingolipid modulation by 4HPR activates a coordinated proteostatic pro-survival response

To mechanistically determine if HSPC require both autophagy and the UPR/ISR for survival in response to SpL modulation with 4HPR in culture, we pharmacologically inhibited autophagy with BAF alone or in combination with ISRIB in lin^- CB. ISRIB is a potent ISR inhibitor by maintaining activity of eIF2B and retaining protein translation despite EIF2α phosphorylation (Hetz et al., 2013). At day 8, the percentage of total number of cells relative to control, $CD34^+$ cells, $CD14^+$ myeloid cells and $GlyA^+$ erythroid cells were quantified by flow cytometry analysis and compared to vehicle (Figure 7A-D). ISRIB appeared to have no significant effect on CB lin^- cells treated with or without 4HPR by the parameters we measured, but significantly decreased proliferation when autophagy was also inhibited. Although BAF treatment was equally potent in restraining proliferation and differentiation particularly to the erythroid lineage in both control and 4HPR treated CB cells, as previously shown in embryonic stem cells and K562 cells (Zyryanova et al., 2018), the addition of ISRIB with BAF significantly limited the number of viable cells and erythroid cells with 4HPR treatment relative to BAF+ISRIB alone and trended to significance in cells treated with 4HPR+BAF relative to 4HPR+BAF+ISRIB (Figure 7A, D). However, BAF treatment in lin^- CB cells was context dependent as addition of BAF at day 2, perhaps when culture-induced stress was lower, had minimal effect on cell growth except for erythroid differentiation (Figure 7E, S7B-F, Laurenti et al., 2015). Finally, lin^- CB cells were treated with same combination of drugs as in Figure 7A beginning at quiescence for 20 hours and then Cyto-ID was used to assess whether autophagic flux activation requires coordinate activation of the UPR/ISR (Figure 7F). As these cells are a mix of stem and progenitor cells, no difference between control and 4HPR-treated cells was observed. However, upon BAF addition to accumulate autolysosomes, a loss of flux demonstrated by an increase in Cyto-ID MFI was observed in 4HPR+BAF cells relative to 4HPR cells alone or control + BAF treated cells (Figure 7F). At this time point, BAF treatment successfully blocked lysosome acidification as measured by flow cytometry with LysoTracker (Figure S7G). Importantly, the accumulation of autolysosomes seen between cells treated with 4HPR+ISRIB and cells treated with 4HPR+ISRIB+BAF was abolished suggesting some aspect of the ISR may be required to activate autophagic flux with 4HPR treatment (Figure 7F). In summary, these data

along with the serial transplantation assays supports a model (Figure 7G) where SpL modulation by 4HPR in *ex vivo* culture activates a coordinated stress response including autophagy and ER stress programs to restore cellular homeostasis and maintain stemness in 4HPR-treated cells during the transition from quiescence to cellular activation.

Discussion

Here, we provide direct evidence that sphingolipid composition regulates HSC self-renewal and lineage commitment. Although short-term culture normally results in marked CD34+ cell expansion at the expense of LT-HSC, our data showed that modulation of SpL metabolism during culture activates cellular stress proteostasis programs that collectively promote the proper metabolic transition from quiescence to cellular activation resulting in LT-HSC maintenance. Four findings emerge from our work: 1) the sphingolipidome has distinct composition within the various mature, progenitor and HSC subsets that comprise the human hematopoietic hierarchy; 2) KD or pharmacological dysregulation of DEGS1 is sufficient to alter the lineage determination of HSPC; 3) dysregulation of Cer and dhCer homeostasis serves as a signal to activate cellular stress proteostasis programs including the UPR and autophagy in human HSPC; and 4) transient SpL modulation by 4HPR during *ex vivo* expansion culture results in the maintenance of functionally defined LT-HSC that possess serial repopulating ability following xenotransplantation.

Membranes are increasingly being recognized as playing central roles in cellular homeostasis and Cer pools have a special role in cellular lipid metabolism (Contreras et al., 2010; Hannun and Obeid, 2018). Here, we establish SpL homeostasis as another aspect of lipid metabolism beyond fatty acid oxidation (Ito et al., 2016) that is pivotal to physiological human hematopoiesis. Cer and the complex SpLs are essential components of multiple cellular membranes including the ER, golgi, mitochondria, lysosomes, autophagosomes and at the plasma membrane (Hannun and Obeid, 2018). Cer is generated either via *de novo* synthesis or from the salvage pathway through catabolic membrane recycling. We found that LT-HSC and ST-HSC favor increased expression of *de* novo synthesis pathway genes compared to more activated progenitors. We undertook sphingolipidome mapping of the human hematopoietic hierarchy and found distinct composition of sphingolipid species between five mature blood lineages and HSPC, particularly around the interface of cer to dhCer homeostasis. By inhibiting the *de novo* SpL metabolic enzyme DEGS1 that adds a double bond to dhCer to form Cer, we modulated these *de novo* Cer pools and found that cellular stress programs were initiated. Our findings point to SpL remodeling as an early event in cellular activation of quiescent HSPC.

Studies from the obesity and aging fields have identified mild induction of ER stress/UPR and autophagy as improving healthspan and lifespan possibly through effects on proteostasis and organelle homeostasis within stem cell populations (Garcia-Prat et al., 2017; Hotamisligil, 2017). Recently, we reported that ATF4 activates the ISR upon amino acid deprivation to increase HSC survival (van Galen et al., 2018). Moreover, physiological aging of HSC appears to result in part through suppression of autophagy programs that maintain metabolic homeostasis (Ho et al., 2017; Mohrin et al., 2015). Whilst a number of ATF4 target genes are known to be involved in

autophagy regulation, the linkage between the UPR, autophagy and ATF4/ISR remains unclear (B'Chir et al., 2013; Lai and Wong, 2008). Our present study points to SpL modulation by 4HPR as a single stimulus that concurrently activates each of these three arms to restore cellular homeostasis following metabolic perturbations such as those occurring during culture. Together, these function as a set of coordinated quality control responses, potentially via a cytoprotective mechanism that promotes the persistence of a more regenerative HSC pool following *ex vivo* cytokine activation from quiescence. We speculate that alterations of Cer/DhCer is part of a "lipid biostat" for stress that is in part enacted by the very distinct biophysical properties of Cer and dhCer. As alluded to in yeast and mouse cells (Thibault et al., 2012), altering lipid homeostasis may have major consequences on membrane structure, and this alteration has been proposed to activate the UPR (Contreras et al., 2010; Halbleib et al., 2017). DEGS1 KD was sufficient to activate the ISR arm of the UPR in HSC subpopulations *in vivo* (Figure 5G-H). Perhaps UPR sensing of various proteostatic and lipostatic stress is blunted during aging and together with erosion of autophagy flux in aged HSC responsible for some aging phenotypes. Would SpL modulation be proficient to activate these cellular stress protection programs and rejuvenate HSC during aging as suggested for rapamycin (Chen et al., 2009; Luo et al., 2014)?

Our data indicate a need to evaluate potential adverse effects of obesity, which is linked to an increase in Cer levels (Turpin et al., 2014), on SpL homeostasis in human hematopoiesis. Obesity is also linked to disruption of the murine bone marrow hematopoietic niche and altering HSC function which persists in cells transplanted from obese mice into a normal environment (Naveiras et al., 2009; Zhou et al., 2017; Lee et al., 2018). We wonder whether obesity reprograms HSC stress responses via SpL lipostatic stress? Moreover, SpL dysregulation is associated with incomplete autophagy in a number of human neuropathies resulting from germline mutations in SpL genes which manifest as lysosomal lipid storage disorders (Hannun and Obeid, 2018). Interestingly, SpL gene expression was higher in neural stem cells than activated progeny, and the lysosome, which serves as a major site for SpL degradation, was proposed to be critical for quality control of neural stem cells during aging (Leeman et al., 2018). Determining the coordination of SpL metabolism, autophagy regulation and lysosomal biogenesis may prove informative for understanding how adult stem cells maintain life-long self-renewal. These data predict that SpL metabolism regulates adult stem function in both blood and brain and perturbation of lipostatic stress sensing in the lysosome or other organelles may contribute to human disease and aging.

The study of HSC stress responses has implications beyond understanding stemness control. The ability to control the cellular properties of human HSC has important clinical implications particularly for HSCT. While 50,000 HSCT procedures occur annually, two thirds of patients who need HSCT lack matched donor tissue (Kiernan et al., 2016; Lund et al., 2015). Limitations of CB as a source for HSCT include the delay in neutrophil recovery following transplantation and long-term sustainability of the donor graft (Lund et al., 2015). We found that DEGS1 inhibition regulates the erythroid-myeloid axis *in vitro*, where there was no alteration of S1P levels, suggesting such lineage commitment changes resulted from dysregulation of SpL composition not S1P signaling. Although we focused on a cell autonomous aspect of this biosynthetic pathway, our results are also consistent with recent work in the field on the role of S1P signaling axes on

lymphoid and erythroid/platelet lineage commitment (Blaho et al., 2015; Vu et al., 2017). We observed a decrease in S1P levels in shDEGS1 cells isolated from the xenograft where there was also disruption of B lymphoid engraftment. Intrinsic genetic perturbation of S1P signaling is sufficient to dysregulate lymphoid commitment and the HSPC hierarchy in mice (Blaho et al., 2015). However, the erythroid to myeloid skewing observed with 4HPR treatment could also result from an ER stress-mediated emergency granulopoiesis-like program (Gombart et al., 2007); this lineage bias may aid in faster neutrophil recovery in patients following transplant of an expanded CB. Another major limitation in wider clinical CB HSCT is the small number of HSC present in a single unit and the inability of many cytokine cocktails to expand LT-HSC. Our studies highlight the metabolic and proteostatic stress perturbations that arise upon cytokine activation that collectively impair LT-HSC function at the expense of generation and expansion of downstream progeny. SpL modulation by 4HPR during *ex vivo* culture activates cytoprotective proteostasis programs that result in preservation of significantly higher numbers of functional LT-HSC in the immunophenotypic HSC pool. Notably, we show here that the search for small molecules to increase LT-HSC donor graft sustainability from CB can be achieved with molecules that do not necessarily expand $CD34^+$ cells. Thus, *ex vivo* CB expansion regimens including 4HPR to activate a lipostatic stress program together with UM171 and SR1 may provide the best compromise between generating large numbers of ST-HSC and progenitors for rapid engraftment while still sparing functional LT-HSC to ensure long-term hematopoiesis.

Acknowledgments

We thank the obstetrics unit of Trillium Health Partners for CB; N. Simard, S. Laronde, T. Velauthapillai, A. Calder, and the UHN-SickKids Flow cytometry facility for cell sorting; A. Murison for RNA-seq data deposition. A. Mitchell, S. Dobson, and J. McLeod for intrafemoral injections; I. Mileva at the Lipidomics Facility of Stony Brook University. We thank Y. Hannun, N. Iscove, D. Sharon, J. Wang, and all members of the Dick lab for critical feedback. E.L. is supported by Wellcome grant 107630/Z/15/Z and a core support grant from the Wellcome and MRC to the Wellcome-Medical Research Council Cambridge Stem Cell Institute. C.L. is supported by U.S. NIH, NCI Grant P01-CA097132. JED is supported by funds from the Princess Margaret Cancer Centre Foundation, Canadian Institutes for Health Research, Joint Canada-Israel Health Research Program, Terry Fox Foundation, and a Canada Research Chair.

Author Contributions

S.Z.X. conceived the study, performed research, analyzed data, and wrote the manuscript; L.P.G., R.F., and E.L. performed research and analyzed data; O.G., E.W., I.P., E.K.L., J.J., and A.V. performed experiments; G.H., G.R., K.P., and M.S. assisted in IF image analysis; K.B.K. performed research and drew the graphical model; L.P.G and S.T. generated the LT-/ST-HSC and GMP RNAseq data set; V.V. performed RNAseq analysis; A.Z. performed scRNAseq analysis; G.B. and E.L. supervised specific experiments; C.L. assisted with lipid measurements; L.P.G., O.G., K.B.K., V.V., E.L., C.L., and J.E.D. edited the manuscript; J.E.D. supervised the study.

Declaration of Interests

The authors declare a patent titled "4HPR and its use in the culturing of hematopoietic stem cells" No. PCT/CA2017/000107 filed May 3, 2017 related to this work.

Figure legends

Figure 1: DEGS1 contributes to the distinct wiring of sphingolipid synthesis in the human hematopoietic hierarchy and is functionally required *in vivo*. (A) Heatmap of mRNA expression for 36 lipid genes that are significantly differentially expressed (FDR <0.05 and fold change >1.5) between LT-HSC and MEP/GMP/CMP/MLP in the dataset from (Laurenti et al., 2013). SpL genes are in bold. (B) SpL distribution in the indicated CB populations (n=3-5). See Figure S1 for direct comparisons of each SpL. (C) Normalized dhCer profiles for stem and progenitor cells with the indicated fatty-acyl chain (n=3). (D) Log2 ratio of Cer to dhCer %. Significance to stem cells in red, to progenitors in blue. (E) qRT-PCR of DEGS1 at 0 hours (h) and 6h in culture from CB subpopulations. (F) Human engraftment ($hCD45^+BFP^+$) at 4 weeks xenotransplantation for shCtrl or shDEGS1 marked by BFP (5 biological replicates, n=5 mice per replicate, see Figure S1J-M for transduction input, hCD45 chimerism, and BFP%). (G) Fold change of BFP marked transduced cells relative to input in human $CD45^+$ cells. Unpaired T-test, p<0.05 (*), p<0.05 (*),01 (**), p<0.01 (**), p<0.001(***).

Figure 2: Sphingolipid modulation of DEGS1 alters HSC function and lineage balance *in vitro*. (A) Total Cer and dhCer levels in lin- CB progeny cultured for 8 days with control or 4HPR (n=2). (B) LT-HSC, ST-HSC, or GMP CFC assays in the presence of ctrl or 2 μM 4HPR showing (B) colonies/100 cells and (C) colony distribution (n=12, CB). Flow cytometry for (D) monocytic (CD14+) and (E) erythroid (GlyA+) markers in live cells from pooled CFC colonies (n=6, CB). (F) Colonly distribution in CFC assays with LT-HSC, ST-HSC, or GMP cells transduced with shCtrl or shDEGS1 (n=4, CB). (G) Flow cytometry for erythroid cells from pooled CFC colonies in Fig 2F. hCD45+BFP+ lacking the $CD34^+CD19^-$ population were isolated from shCtrl or shDEGS1 mice at 4 weeks post-transplant (n=2 CB) and profiled by LC/MS for (H) total Cer and dhCer levels and (I) normalized Cer and dhCer profiles with the indicated fatty-acyl chain. p<0.05 (*), p<0.01 (**), p<0.001(***).

Figure 3: *Ex vivo* treatment with 4HPR maintains HSC function following xenotransplantation. (A) Experimental scheme for *ex vivo* culture of lin^- CB followed by xenotransplantation with vehicle control or 4HPR. (B) Total cell counts at 8 days culture for the 16 LTRC dose of a representative experiment (n=3, CB cultured in triplicate). The number of (C) viable cells, (D) $CD15^+$ myeloid cells, (E) $GlyA^+$ erythroid cells, and (F) $CD34^+$ cells injected/mouse were calculated for the 16 LTRC dose by flow cytometry analysis for control or 4HPR treatment prior to xenotransplantation (n=5 CB pools, 4 in technical triplicate, marked with different symbols). (G) Human $CD45^+$ engraftment at 16 weeks post-transplant in injected femurs and non-injected bones (n=4 CB pools, 5 mice/drug treatment for each CB pool). Lineage analysis of mice engrafted with control or 4HPR-treated cells from figure 2G for (H) B lymphoid, (I) myeloid, (J) erythroid, and (K) $CD34^+$ lacking CD33 or CD19 markers at the 16 LTRC dose. p<0.05 (*), p<0.01 (**),

p<0.001(***).

Figure 4: Sphingolipid modulation restricts expansion of committed progenitors during *ex vivo* culture to enhance HSC self-renewal. (A) Number of colonies for LT-HSC CFC assays with control (-) or the indicated combination of 4HPR, UM171 or SR1 at 10 days, unpaired t-test relative to control (ctrl, black) or to the presence or absence of 4HPR treatment. (B) Flow cytometry for the % and count (#) of CD34+ cells subsequently transplanted per mouse following 8 days culture. (C) Representative flow cytometry plots for CD90 and CD45RA within the $CD34^+$ fraction of lin^- CB progeny at day 8 with the indicated treatments. (D) Distribution of cultured $CD34^+CD90^+CD45RA^-$ (cLT), $CD34^+CD90^-CD45RA^-$ (cST), and $CD34^+CD90^-CD45RA^-$ (cProg) for the treatments at day 8 following CD34 enrichment (n=4), unpaired t-test relative to control. (E-F) $CD45^+$ cells were isolated from 16 LTRC dose mice and transplanted at limiting doses into secondary recipients for 16 weeks and combined to calculate LTRC frequencies (5 biological experiments for control and 4HPR; 2 biological experiments for U+S and 3-Factor). Human CD45+ marking of >0.1% was considered positive for secondary engraftment. P-value was by ELDA. p<0.05 (*), p<0.01 (**), p<0.001(***).

Figure 5: Sphingolipid modulation with 4HPR treatment upregulates cellular stress pathways and remodels cellular metabolism in HSPC during *ex vivo* culture. (A) NES scores for selected pathways that are significantly enriched following 4HPR treatment at day 2. (B) Pathway analysis (GSEA) of SpL/cer, cholesterol biosynthesis ERstress/UPR, protein folding and ROS pathway modules for 4HPR compared to control. (C) GSEA analysis of autophagy, ER stress/UPR, protein folding or ROS pathways in uncultured LT-HSC vs ST-HSC. (D-E) LT-HSC from Velten, et al. were clustered as cell cycle-primed or non-primed as described in methods (D) the gene expression of CDK6 (top) and DEGS1 (bottom), and (E) Signature scores representing relative expression of pathways in 5C for single LT-HSCs, Wilcoxon rank sum test for 5D-E, p<0.05 (*), p<0.01 (**), p<0.001(***), p<0.0001 (****). (F) Heatmap showing gene expression at day 2 of the top 4 genes in gene sets in 5A organized as pathways. We included ATF4 related genes gene sets from the ER stress/UPR pathway. Median pEIF2S1 staining intensity quantified from microscopy images for BFP^+ (G) LT-HSC and (H) ST-HSC isolated from 4 week xenografts engrafted with shCtrl or shDEGS1 stem cells for 3 CBs (60 cells/CB, except shDEGS1 LT-HSC, 13-17 cells/CB). Flow cytometry analysis at day 2 post-treatment with indicated concentrations of 4HPR in the progeny of $CD34^+CD38^-$ stem or $CD34^+CD38^+$ progenitor CB cells from 4 CBs for (I) ROS with CellROX and (J) mitochondrial membrane potential with TMRE. Paired t-test, p<0.05 (*), p<0.01 (**), p<0.001(***) in 5G-J.

Figure 6: 4HPR activates autophagy in HSPC during *ex vivo* culture. LC3II staining intensity of (A) LT-HSC (174 cells) and GMP (312 cells) isolated from CB (n=3) or (B) mPB (165 cells, n=3 mPB) LT-HSC compared to CB LT-HSC. (C) Representative microscopy images of DAPI (blue) and LC3II staining (green) for (C)CD34+CD38- (stem) cells following 2 days of treatment with DMSO control or 2uM 4HPR and $\pm$ BAF. Scale is 5 μm. LC3II foci area for (D) stem and (E) prog cells from one of three CB. The mean in control stem cells without BAF is shown with a dotted line. (F) Relative LC3II foci in the presence of BAF for stem and Prog populations. (G) Relative cyto-ID flux for 0 (DMSO), 0.2 uM and 2 uM 4HPR in stem and prog populations at 2 days post-treatment (n=4). (H) Relative CytoID MFI measurements for stem-enriched samples to analyze autophagic flux

with and without cytokine withdrawal with indicated drug treatments at day 2. $p<0.05$ (*), $p<0.01$ (**), $p<0.001$(***).

Figure 7: Sphingolipid modulation by 4HPR activates a coordinated proteostatic pro-survival response. Flow cytometry analysis at day 8 culture following autophagy inhibition with BAF and/or ISR inhibiton with ISRIB in lin^- CB (n=3, in duplicate) beginning at Day 0 for control or 4HPR treated cells for number of (A) live cells (B) $CD34^+$ cells (C) $CD14^+$ cells and (D) $GlyA^+$ cells; represented as relative % to control, mean +/- SEM. (E) Total number of cells at day 8 after BAF was added either starting at day 0 or day 2. (F) Autophagic flux at 20 hours with indicated drugs was assayed with Cyto-ID MFI relative to control (2 CB, in triplicate). (G) Model for how 4HPR maintains stemness during *ex vivo* culture. $p<0.05$ (*), $p<0.01$ (**), $p<0.001$(***).

STAR METHODS

LEAD CONTACT AND MATERIALS AVAILABILITY

Further information and requests for resources and unique/stable reagents generated in this study should be directed to and are available without restriction from the Lead Contact, John E. Dick (jdick@uhnresearch.ca).

METHODS DETAILS

EXPERIMENTAL MODEL AND SUBJECT DETAILS

Human cord blood samples were obtained with informed consent from Trillium and Credit Valley Hospital according to procedures approved by the University Health Network (UHN) Research Ethics Board. Mononuclear cells were obtained by centrifugation on Lymphoprep medium (Stem Cell Technologies) and were depleted of Lin+ cells (lineage depletion) by negative selection with the StemSep Human Progenitor Cell Enrichment Kit according to the manufacturer's protocol (Stem Cell Technologies). Lin^- CB cells were stored viably at -80°C or -150°C. Human mobilized peripheral blood samples (mPB) were obtained with informed consent from Princess Margaret Cancer Centre according to procedures approved by the UHN Research Ethics Board. Following mononuclear cell isolation, CD34+ cells from CB and mPB were enriched by positive selection with the CD34 Microbead kit (Miltenyi) and LS column purification with MACS magnet technology (Miltenyi).

CELL SORTING

Lin^- cells were thawed by dropwise addition of X-VIVO + 50% fetal calf serum supplemented with DNase (100μg/mL final concentration, Roche) and resuspended at a density of 5×10^6 cells/mL. Cells were then stained with the following antibodies (all from BD, unless stated otherwise): FITC–anti-CD45RA (1:50, 555488), PE–anti-CD90 (1:50, 555596), PECy5–anti-CD49f (1:50, 551129), V450–anti-CD7 (1:33.3, 642916), PECy7–anti-CD38 (1:200, 335790), APC–anti-CD10 (1:50, 340923), APCCy7–anti-CD34 (1:200, custom made by BD). Cells were sorted on FACS Aria III (Becton Dickinson), consistently yielding >95% purity. LT-HSC were sorted based on the following markers: $CD34^+CD38^-CD45RA^-CD90^+CD49f^+$. ST-HSC were sorted as $CD34^+CD38^-CD45RA^-CD90^-CD49f^-$ and GMP as $CD34^+CD38^+CD10^-CD7^-CD45RA^+$. shCtrl or shDEGS1 previously frozen 4 week xenograft samples were thawed as described above. Mouse cells were depleted with the mouse depletion kit (Miltenyi) and LS column purification with MACS magnet technology (Miltenyi). Cells were then stained with the following primary antibodies: FITC–anti-CD45RA PE–anti-CD90, PECy5–anti-CD49f, BV711-CD19 (1:50, 563036), Alexafluor700–anti-CD7 (1:50, 561603), either APC–anti-CD10 or Alexafluor700–anti-CD10 (1:50, 563500) BV510-CD45 (1:50, 563891), biotin-Flt3L (1:50, 624008), and APCCy7–anti-CD34. Cells were washed and then stained with streptavidin-Qdot605 (1:100, Q10101MP). LT-HSC were sorted based on the following markers: $CD45^+BFP^+C19^-CD34^+CD38^-CD45RA^-CD90^+CD49f^+$. ST-HSC were sorted as $CD45^+BFP^+CD19^-CD34^+CD38^-CD45RA^-CD90^-CD49f^-$ and GMP as $CD45^+BFP^+CD19^-CD34^+CD38^+CD10^-CD7^-CD45RA^+$.

SPHINGOLIPID QUANTITATION BY MASS SPECTROMETRY

To profile the SpL composition of primitive CB cells, 1.05-1.1 million CD34+CD38- and 1.9-2.9 million $CD34^+CD38^+$ cells were isolated from 3 pools of previously frozen lin- CB (22 million – 50 million cells) by flow cytometry, washed with PBS, and frozen as cell pellets. For the SpL distribution of mature CB lineages, freshly isolated CB bags from five individuals were processed for mononuclear cells and a small fraction stained with V450-anti-CD15, APC-cy7-anti-CD34, PE-Cy7-anti-GlyA, PECy5–anti-CD14, FITC-anti-CD3, and V500-anti-CD45 to sort for erythrocytes (GlyA+CD45-) prior to ammonium chloride lysis. After lysis, cells were stained at 10 million/ml and T cells ($CD45^+CD3^+CD19^-CD14^-CD15^-$), B Cells ($CD45^+CD3^-CD19^+CD14^-CD15^-$), monocytes ($CD45^+CD3^-CD19^-CD14^+CD15^-$), and neutrophils ($CD45^+CD3^-CD19^-CD14^-CD15^+$) were isolated by flow cytometry on the Aria Fusion or Aria RITT. Cell numbers ranged from 1-4 million cells. Subsequent lipid extraction and mass spectrometry for sphingomyelin species, hexosylceramide species, ceramide species, dihydroceramide species and sphingoid species were performed by the Lipidomics Facility of Stony Brook University Medical Center (Bielawski et al., 2009). As the morphology between the subpopulations are quite distinct, particularly between the mature lineages, normalization of the sphingolipidome data was an important consideration. Normalization to cellular inorganic phosphate (P_i) was chosen to minimize the potential confounding effects of differences in cellular size and protein content between the profiled populations. Two pools CD34- lin^- CB cultured with DMSO control or 4HPR for 8 days were collected and 4 million expanded cells were washed twice in PBS and frozen as cell pellets. $CD45^+BFP^+$ cells lacking the $CD34^+CD19^-$ population were sorted from shCtrl (1.8-2.7 million cells) or shDEGS1 (0.4-0.5 million cells) previously frozen 4 week xenograft samples (Primary transplant data in Figure S1I-O, Experiment 1, n=2 biological replicates), washed and frozen as cell pellets. Subsequent lipid extraction and mass spectrometry for ceramide species, dihydroceramide species and sphingoid species were performed by the Lipidomics Facility of Stony Brook University Medical Center. Inorganic phosphate levels were measured for lipid normalization across samples.

LENTIVIRAL SHRNA KNOCK-DOWN OF DEGS1

shRNA sequences were predicted using the Sherwood algorithm (Knott et al., 2014) and ordered as Ultramer DNA oligos (IDT). Subsequently, shRNAs were amplified using AmpliTaq Gold 360 Polymerase (ThermoFisher, 4398813) using FW primer: 5'-GGATCCTGTTTGAATGAGGCTTCAGTACTTTACAGAATCGTTGCCTGCACATCTTGGAAACACTTGCTGGGATTACTTCT-3' and RV primer: 5'-AGTAACGCGTAAAGTGATTTAATTTATACCATTTTAATTCAGCTTTGTAAAAATGTATCAAAGAGATAGCAAGGTATTCAGTTTTAGTAAACAAGATAATTGCTCCTAAAGTAGCCCCTTGAAGTCCGAGGCAGTAGGCA-3'. The PCR product was digested with BamH1-HF and Mlu1-HF (NEB) and subcloned into the pLBC2 lentiviral vector, downstream of SFFV-tBFP. Viral production, titration and transduction of $CD34^+CD38^-$ CB cells were done as previously described (Kaufmann et al., 2019).

<u>shRNA sequences:</u>

DEGS1 shRNA (shDEGS1):

5'-TGCTGTTGACAGTGAGCGAGGTCATGAAACTTACTCATAATAGTGAAGCCACAGATGTATTATGAGTAAGTTTCATGACCCTGCCTACTGCCTCGGA-3'

control Renilla shRNA (shCtrl):
5'-
TGCTGTTGACAGTGAGCGCAGGAATTATAATGCTTATCTATAGTGAAGCCACAGATGTATAGATAAGCA
TTATAATTCCTATGCCTACTGCCTCGGA-3'

QUANTITATIVE RT-PCR FOR DEGS1 KNOCKDOWN

In order to assess shRNA knock-down efficiency, MOLM13 cells were infected at a multiplicity of infection of 0.3. Transduced cells were sorted for BFP^+ expression and total RNA was isolated and DNAse treated using the RNeasy Micro Kit (Qiagen, 74004). RNA quality (RIN > 9) was verified using the Bioanalyzer RNA 6000 Pico Kit (Agilent) and cDNA was synthesized using SuperScript VILO (ThermoFisher, 11754050). qPCR was performed on the Roche Lightcycler 480 using Power SYBR Green (ThermoFisher, 4367659). All signals were quantified using the ΔCt method and were normalized to the levels of GAPDH.

qPCR primers:
DEGS1:
5'-CAAACATTCCAAACCAGCGAT-3'
5'-GCAGTTGCATTAACCACTCAA-3'
GAPDH:
5'-ACATCGCTCAGACACCATG-3'
5'-TGTAGTTGAGGTCAATGAAGGG-3'

XENOTRANSPLANTATION

All animal experiments were done in accordance to institutional guidelines approved by the University Health Network Animal care committee. Aged match female or male NSG mice (NOD.Cg *Prkdc*scid*Il2rg*tm1Wjl /SzJ; Jackson Laboratory) 10-12 weeks of age were sublethally irradiated with 250 rads 1 day before intrafemoral injection. Following 4 weeks xenotransplantion of lentiviral DEGS1 knockdown into male NSG, mice were euthanized and the injected femur and other bones were flushed separately in Iscove's modified Dulbecco's medium (IMDM) and human chimerism and transduced cells marked by BFP expression were assessed by flow cytometry on the BD Celesta and the following antibodies: PE–anti-CD19 (349209), PE–anti-GlyA (Beckman Coulter, A07792), V500–anti-CD45 (560777), APCCy7–anti-CD34, and BV786–anti-CD33 (740974). For primary transplant analysis of *ex vivo* cultured cells, female mice were euthanized at 16 weeks after transplantation. The injected femur and other bones were flushed separately in Iscove's modified Dulbecco's medium (IMDM) and human chimerism was assessed with the following antibodies: PE–anti-CD19 (349209), PE–anti-GlyA (Beckman Coulter, A07792), PECy5–anti-CD45 (Beckman Coulter, A07785), PECy7–anti-CD14 (1:200; Beckman Coulter, A22331), APC–anti-CD33 (551378) and V450–anti-CD15 (642917). For secondary LDA assays, primary transplant mice from each treatment group were individually thawed, and 1/3 of each mouse pooled and stained with APC–anti-CD45 and FITC–anti-CD45. Human CD45+ cells were sorted from each pooled sample and injected at indicated doses into irradiated female NSG mice and engraftment assessed at 16 weeks post-transplant. For LDA experiments, injected femur and non-injected femurs were isolated and flushed separately and analyzed with the following: APC–anti-CD45, FITC–anti-CD45, PE-anti-CD19 and APC–anti-CD33. A mouse was considered

engrafted if CD45+>0.1 and multilineage. LTRC frequency was estimated using the ELDA software (http://bioinf.wehi.edu.au/software/elda/; (Hu and Smyth, 2009). The remaining 2/3 of bone marrow from each individual mouse was first enriched for CD34+ cells by positive selection with the CD34 Microbead kit (Miltenyi) and LS column purification with MACS magnet technology (Miltenyi). CD34+ enriched cells were then directly analyzed by flow cytometry with the following antibodies: FITC–anti-CD45RA, APC–anti-CD90, PECy5–anti-CD49f, V450–anti-CD7, PECy7–anti-CD38, V421–anti-CD10, APCCy7–anti-CD34, PE-anti-CD19, V500-anti-CD45.

METHYLCELLULOSE CFC ASSAY

LT-HSC, ST-HSC, or GMP were sorted directly into methylcellulose (cat. No H4034, Stem Cell Technologies), supplemented with FLT3 Ligand (20 ng/ml) and IL6 (50 ng/ml). Fenretinide/4HPR (Tocris Biosciences, cat. # 1396), StemRegenin1 (Stem Cell Technologies, cat. # 72344), and UM171 (Xcessbio, cat. #60223-2), or DMSO vehicle were added following sorting at the following concentrations, DMSO (control), 2μM 4HPR, 35nM UM171 or 500 nM SR1, such that DMSO was always <0.1% and equal between treatment and control groups. ATRA was a kind gift from G. Keller. Samples were mixed and plated onto 35 mm dishes in duplicates. Colonies were allowed to differentiate for 10-11 days and morphologically assessed for colonies in a blind fashion by a second investigator. At day 14, colonies from replicate plates were pooled and resuspended in PBS/FBS and stained with FITC–anti-CD45RA, APC–anti-CD90, PECy5–anti-CD14, APCCy7–anti-CD34, PE-anti-CD235a (GlyA) for flow cytometry analysis on a BD Canto or Celesta. For shDEGS1 experiments, sorted LT-HSC, ST-HSC, or GMP were cultured in low cytokine media for 4 hours and then transduced with shCtrl or shDEGS1 lentivirus. At day 3 post-transduction, BFP+ cells were sorted directly into methylcellulose as above for colony scoring 10 days later (day 13 post-transduction). At day 16 post-transduction, colonies were analyzed on the Celesta for BFP and with APC–anti-CD90, PECy5–anti-CD14, APCCy7–anti-CD34, PE-anti-GlyA, and BV786–anti-CD33.

***EX VIVO* CORD BLOOD CULTURE SCHEME**

Lin^- CB were thawed via dropwise addition of X-Vivo based thawing media (X-Vivo, 50% FBS+1% DNAse), resuspended in cytokine media, viable cells counted, and placed into appropriate cell concentrations for liquid culture (Laurenti et al., 2015): StemPro (Stem Cell Technologies) supplemented with StemPro nutrients (Stem Cell Technologies), L-glutamine (GIBCO), Pen/Strep (GIBCO), human LDL (Stem Cell Technologies, 50 ng/mL) and the following cytokines (all from Miltenyi): SCF (100 ng/mL), Flt3L (20 ng/mL), TPO (100 ng/mL), IL-6 (50 ng/mL), IL-3 (10 ng/mL), GM-CSF (20 ng/mL), except EPO (3 units/mL, from Jansen). The experimental scheme for *ex vivo* culture of viable lin- CB cells post thawing is the following: 3 initial cell doses in a LDA fashion with 62,500 cells (high), 12,500 cells (medium), and 2,500 cells (limiting) are cultured per well in a 24 well plate with 0.5 mls expansion media plus vehicle control or drug(s) on day 0. We mimicked fed-batch growth conditions where drug was added with fresh media every second day for 8 days to reduce auto-inhibitory signalling and ensure nutrients and drugs are not limiting during the culture period (Csaszar et al., 2012): fresh media plus drugs are added on day 2 (0.5 mls), day 4 (1 ml), and feeding and transferring to a 6 well plate on day 6 (2 mls). On day 8, all progeny are collected and $10/11^{th}$ are unbiasly transplanted via intrafemoral injection into 5 NSG mice/condition. 1 LTRC cell is roughly equivalent to 700 lin- CB cells as previously calculated in xenotransplantation (Notta et al., 2011). This translates to the equivalent of the following day 0

cell doses: ~11,300 lin- cells or ~16 initial LTRC/mouse (high), ~2270 lin- cells or~3.2 LTRC/mouse (medium) and 454 lin- cells or ~0.65 LTRC/mouse (limiting). The remaining $1/11^{th}$ of day 8 progeny are analyzed by flow cytometry on a BD canto with a plate reader to enumerate cell numbers and lineage distribution with the following: V450-anti-CD15, APC-cy7-anti-CD34, PE-Cy7-anti-GlyA, PECy5–anti-CD14, or FITC-anti-CD15, PE-Cy5-anti-CD34, PE-anti-GlyA, PECy7–anti-CD14. LT-HSC, ST-HSC and GMP were sorted and ~500 cells/well were cultured in 100 μl of cytokine media with DMSO on a 96 well plate on day 0. On day 4, an additional 100 μl of *ex vivo* media with compounds were added. Cells were stained with APCCy7–anti-CD34 on day 8 on a BD Canto with plate reader. For inhibition of autophagy and the ISR, 20nM Bafilomycin A1 (Sigma, B1793) and 500 nM ISRIB (Selleckchem, S7400), dissolved in DMSO, were added to 20,000 lin- CB cultured in cytokine media as indicated and analyzed for viable cells and lineage as previously and with CytoID (Enzo Life Sciences) or LysoTracker blue (ThermoFisher Scientific, L7525).

PROLIFERATION AND CELL CYCLE ANALYSIS ASSAYS

For assessment of proliferation using BrdU incorporation assays, indicated subpopulations were cultured for three days with DMSO vehicle or 2μM 4HPR in expansion media when BrdU was added to cells for 4 to 8 hours. BrdU staining was performed with the APC BrdU Flow Kit (BD Pharmingen) with APC-anti-BrdU according to the manufacturer's protocol. Sorted LT-HSC, ST-HSC or GMP were cultured in *ex vivo* culture media with vehicle or 4HPR as indicated and fixed and stained for Ki67-Hoechst assays as described (Laurenti et al., 2015). LT-HSC and GMP were sorted from shCtrl or shDEGS1 previously frozen 4 week xenograft samples (Primary transplant data in Figure S1I-O, Experiment 1, n=2 CB) and fixed and stained for Ki67-Hoechst analysis. Samples were analyzed on a BD LSRII cytometer with an UV laser.

IMMUNOFLUORESCENCE FOR LC3II AND PHOSPHORYLATED EIF2α

$1x10^4$ sorted CD34+CD38- or CD34+CD38+ cells were cultured in *ex vivo* culture media on a 96 well suspension plate with DMSO or 2μM 4HPR. Bafilomycin A1 was added at 30 hours post-culture. Cells were collected at 48 hours post-culture and fixed with 4% paraformaldehyde. Cells were stain with a mouse monoclonal antibody to LC3II (NanoTools, 5F10) and DAPI. Slides were visualized on a Zeiss LS700 confocal microscope and images collected. Quantitation of LC3II foci area as a percentage of total cell area was done using R and Image J software (n=3 CB). A range of 50-150 cells were quantified per condition. LT-HSC and GMP were purified sorted from $CD34^+$ CB or mPB samples, fixed with 4% paraformaldehyde and stained with LC3 and DAPI as above. Following image collection on a Zeiss LS700 confocal microscope, LC3II integrated density (total signal intensity) was quantified using R and Image J software (n=3). LT-HSC and ST-HSC were sorted from shCtrl or shDEGS1 previously frozen 4 week xenografts samples (n=3, Experiment 2, Figure S1I-O), fixed with 4% paraformaldehyde and stained with a rabbit monoclonal antibody to EIF2S1 (phospho S51, Abcam, ab196460) and DAPI and images collected as above.

CYTOID, ROS, MITOCHONDRIA MEMBRANE POTENTIAL ANALYSIS

$1x10^4$ sorted $CD34^+CD38^-$ or $CD34^+CD38^+$ cells were cultured in *ex vivo* media on a 96 well suspension plate with DMSO, 0.2μM or 2μM 4HPR for either 2 days or 3 days. Autophagy flux was measured using CytoID analysis kit (Enzo Life Sciences). Cytokine withdrawal experiments to

induce autophagy were done by replacing media containing only drugs without cytokines for 6 hours on cells and then analyzing with CytoID. Staining for ROS and mitochondrial membrane potential in active mitochondria was performed by incubating cells at 37 °C with 5 µM CellROX deep red (C10422) and 1 µM TMRE (T668), following the manufacturer's protocols (ThermoFisher) and directly analyzed on a BD celesta.

RNA-SEQUENCING AND PATHWAY ANALYSIS

Three pools of lin- CB at the 16 LTRC dose (62,500 cells/well, 24 well plate) were cultured with *ex vivo* culture media and the following 4 treatment conditions: DMSO (control), 2µM 4HPR, 35nM UM171 + 500 nM SR1 (U+S) or combination of 4HPR+UM171+SR1 (3-Factor). Cultured cells at day 2 and day 4 were collected, pelleted, washed twice with PBS and resuspended in RNeasy microRNA plus kit (Qiagen) and frozen for subsequent RNA isolation. Sufficient cells were cultured to isolate a minimum of 500 ng RNA. Nextera libraries were generated without amplification and subjected to 125 bp, paired-end RNA-sequencing on the Illumina HiSeq 2500 with an average of ~57 million reads/sample at the Center for Applied Genomics, Sick Kids Hospital. Reads were trimmed to remove the adapters and were then aligned to hg19 using TopHat (v2.1.1) and gene counts were generated using HTSeq (v 0.6.1). Read counts were retrieved for each sample and processed using edgeR to estimate differential expression between the treated and ctrl samples and between 3-Factor and U+S and 4HPR. Genes with count per million equal or less than 0.25 in at least one fifth of the samples were removed from further analysis. 15085 genes remained in the analysis. edgeR dispersion parameters were estimated for the whole dataset and a generalized model was applied to compare each treated-control pair. Cord blood batch was included in the model. Tests were corrected for multiple hypothesis testing using the Benjamini-Hochberg method. MDS plots, hierarchical clustering and heatmaps were generated using logarithm of base2 of count per million of TMM normalized counts. A score to rank genes from top up-regulated to down-regulated was calculated using the formula -sign(logFC) * -log10(pvalue). The rank file from each comparison was used in pathway analysis (GSEA) (http://software.broadinstitute.org/gsea/index.jsp) using 2000 permutations and default parameters against a pathway database containing Msigdb c2 and c3, NCI, IOB, NetPath, HumanCyc, GO BP and Panther (http://baderlab.org/GeneSets, version April 2017). NES and FDR results are located in Table S1. EnrichmentMap version 2.1.0 in Cytoscape 3.4.0 was used to visualize enriched pathway gene sets at FDR <= 0.05 with a Jaccard coefficient set to 0.25. For GSEA analysis in Figure 5B and Velten, et al. scRNA-seq, lists of genes were returned by taking the union of all gene sets for the pathways in Figure 5A.

SINGLE CELL RNA-SEQ ANALYSIS

Index-sorted single cell (sc) RNA-seq data of human HSPCs (Velten et al., 2017) were obtained from GEO (GSE75478). Raw count data and FACS surface marker annotations were loaded into the Scanpy single cell analysis suite (Wolf et al., 2018). FACS surface marker measurements were subject to logicle transformation through the flowutils package (https://github.com/whitews/FlowUtils), and used to distinguish $CD34^+CD38^-$ plates from $CD34^+CD38^+$ plates for each individual. Among the $CD34^+CD38^-$ plates, $CD34^+CD38^-CD45RA^-$ HSPCs were identified and their gene expression counts were subjected to pooling normalization using the scran package in R (Lun et al., 2016). Normalized $CD34^+CD38^-CD45RA^-$ HSPCs for each

individual were subsequently clustered using the 'Self Assembling Manifolds' (SAM) algorithm, which iteratively re-scales gene expression to identify subpopulations with subtle, yet consistent, differences (Tarashansky et al., 2018). SAM returned two distinct clusters for each individual, with one cluster demarcated by higher CDK6 expression, expression of cell cycle genes (Tirosh et al., 2016), and surface CD38 expression as measured through FACS. Cells in the second cluster expressed fewer distinct genes but displayed higher relative expression of genes associated with HSC dormancy from murine studies (Cabezas-Wallscheid et al., 2017, using genes with logFC>2 and FDR<0.01 in dHSC vs aHSC and MPP). We thus labeled the clusters 'cell cycle-primed' and 'non-primed', respectively. Among $CD34^{+}38^{-}45RA^{-}$ cells from both individuals, we confirmed that the cell cycle-primed cluster had significantly higher expression of DEGS1 and of genes associated with ER Stress/UPR and protein folding, but comparable expression for genes associated with ROS and autophagy, consistent with our results for LT-HSCs. Signature scores for gene expression programs were derived by comparing the relative expression of that gene set with a random set of genes in the transcriptome (Tirosh et al., 2016) as implemented in Scanpy. LT-HSC were represented in both the cell cycle-primed cluster and the non-primed cluster. To examine LT-HSC specifically, we identified $CD34^{+}38^{-}45RA^{-}$ cells that were within the top 40^{th} percentile for both CD49f and CD90 surface marker expression.

STATISTICAL ANALYSES

GraphPad Prism was used for all statistical analyses except RNA-seq. Unless otherwise indicated, mean +/- SD values are reported in the graphs. Statistical significance was determined with Student t-tests. $p<0.05$ (*), $p<0.01$ (**), $p<0.001$(***), and $p<0.0001$(****).

DATA AND CODE AVAILABILITY

Processed RNA-seq data is available on GEO under accession numbers GSE125214 (4HPR) and GSE125345 (uncultured LT-HSC, ST-HSC and GMP). Raw data is available on EGA under accession number EGAS00001003756.

.

References

Amirache, F., Lévy, C., Costa, C., Mangeot, P.-E., Torbett, B.E., Wang, C.X., Nègre, D., Cosset, F.-L., and Verhoeyen, E. (2014). Mystery solved: VSV-G-LVs do not allow efficient gene transfer into unstimulated T cells, B cells, and HSCs because they lack the LDL receptor. Blood *123*, 1422.

Atilla-Gokcumen, G.E., Muro, E., Relat-Goberna, J., Sasse, S., Bedigian, A., Coughlin, M.L., Garcia-Manyes, S., and Eggert, U.S. (2014). Dividing cells regulate their lipid composition and localization. Cell *156*, 428-439.

B'Chir, W., Maurin, A.C., Carraro, V., Averous, J., Jousse, C., Muranishi, Y., Parry, L., Stepien, G., Fafournoux, P., and Bruhat, A. (2013). The eIF2alpha/ATF4 pathway is essential for stress-induced autophagy gene expression. Nucleic Acids Res *41*, 7683-7699.

Bielawski J, Pierce JS, Snider J, Remibiesa B, Szulc ZM, Bielawska A. (2009) Comprehensive quantitative analysis of bioactive sphingolipids by high-performance liquid chromatography-tandem mass spectrometry. *Methods Mol Bio*. *579*, 443-67.

Blaho, V.A., Galvani, S., Engelbrecht, E., Liu, C., Swendeman, S.L., Kono, M., Proia, R.L., Steinman, L., Han, M.H., and Hla, T. (2015). HDL-bound sphingosine-1-phosphate restrains lymphopoiesis and neuroinflammation. Nature *523*, 342-346.

Buenrostro, J.D., Giresi, P.G., Zaba, L.C., Chang, H.Y., and Greenleaf, W.J. (2013). Transposition of native chromatin for fast and sensitive epigenomic profiling of open chromatin, DNA-binding proteins and nucleosome position. Nat Meth *10*, 1213-1218.

Burgos-Barragan, G., Wit, N., Meiser, J., Dingler, F.A., Pietzke, M., Mulderrig, L., Pontel, L.B., Rosado, I.V., Brewer, T.F., Cordell, R.L*., et al.* (2017). Mammals divert endogenous genotoxic formaldehyde into one-carbon metabolism. Nature *548*, 549-554.

Cabezas-Wallscheid, N., Buettner, F., Sommerkamp, P., Klimmeck, D., Ladel, L., Thalheimer, F.B., Pastor-Flores, D., Roma, L.P., Renders, S., Zeisberger, P*., et al.* (2017). Vitamin A-Retinoic Acid Signaling Regulates Hematopoietic Stem Cell Dormancy. Cell.

Campbell, M.R., Karaca, M., Adamski, K.N., Chorley, B.N., Wang, X., and Bell, D.A. (2013). Novel Hematopoietic Target Genes in the NRF2-Mediated Transcriptional Pathway. Oxidative Medicine and Cellular Longevity *2013*, 120305.

Chen, C., Liu, Y., Liu, Y., and Zheng, P. (2009). mTOR Regulation and Therapeutic Rejuvenation of Aging Hematopoietic Stem Cells. Science Signaling *2*, ra75-ra75.

Contreras, F.X., Sánchez-Magraner, L., Alonso, A., and Goñi, F.M. (2010). Transbilayer (flip-flop) lipid motion and lipid scrambling in membranes. FEBS Letters *584*, 1779-1786.

Csaszar, E., Kirouac, D.C., Yu, M., Wang, W., Qiao, W., Cooke, M.P., Boitano, A.E., Ito, C., and Zandstra, P.W. (2012). Rapid expansion of human hematopoietic stem cells by automated control of inhibitory feedback signaling. Cell Stem Cell *10*, 218-229.

Dahm, F., Nocito, A., Bielawska, A., Lang, K.S., Georgiev, P., Asmis, L.M., Bielawski, J., Madon, J., Hannun, Y.A., and Clavien, P.A. (2006). Distribution and dynamic changes of sphingolipids in blood in response to platelet activation. Journal of Thrombosis and Haemostasis *4*, 2704-2709.

Donoviel, M.S., Hait, N.C., Ramachandran, S., Maceyka, M., Takabe, K., Milstien, S., Oravecz, T., and Spiegel, S. (2015). Spinster 2, a sphingosine-1-phosphate transporter, plays a critical role in inflammatory and autoimmune diseases. FASEB J *29*, 5018-5028.

Doulatov, S., Notta, F., Laurenti, E., and Dick, John E. (2012). Hematopoiesis: A Human Perspective. Cell Stem Cell *10*, 120-136.

Fares, I., Chagraoui, J., Gareau, Y., Gingras, S., Ruel, R., Mayotte, N., Csaszar, E., Knapp, D.J., Miller, P., Ngom, M.*, et al.* (2014). Cord blood expansion. Pyrimidoindole derivatives are agonists of human hematopoietic stem cell self-renewal. Science *345*, 1509-1512.
Gan, B., Hu, J., Jiang, S., Liu, Y., Sahin, E., Zhuang, L., Fletcher-Sananikone, E., Colla, S., Wang, Y.A., Chin, L.*, et al.* (2010). Lkb1 regulates quiescence and metabolic homeostasis of haematopoietic stem cells. Nature *468*, 701-704.
Garcia-Prat, L., Sousa-Victor, P., and Munoz-Canoves, P. (2017). Proteostatic and Metabolic Control of Stemness. Cell Stem Cell *20*, 593-608.
Golan, K., Vagima, Y., Ludin, A., Itkin, T., Cohen-Gur, S., Kalinkovich, A., Kollet, O., Kim, C., Schajnovitz, A., Ovadya, Y.*, et al.* (2012). S1P promotes murine progenitor cell egress and mobilization via S1P1-mediated ROS signaling and SDF-1 release. Blood *119*, 2478-2488.
Gombart, A.F., Grewal, J., and Koeffler, H.P. (2007). ATF4 differentially regulates transcriptional activation of myeloid-specific genes by C/EBPepsilon and C/EBPalpha. J Leukoc Biol *81*, 1535-1547.
Gurumurthy, S., Xie, S.Z., Alagesan, B., Kim, J., Yusuf, R.Z., Saez, B., Tzatsos, A., Ozsolak, F., Milos, P., Ferrari, F.*, et al.* (2010). The Lkb1 metabolic sensor maintains haematopoietic stem cell survival. Nature *468*, 659-663.
Haas, S., Trumpp, A., and Milsom, M.D. (2018). Causes and Consequences of Hematopoietic Stem Cell Heterogeneity. Cell Stem Cell *22*, 627-638.
Halbleib, K., Pesek, K., Covino, R., Hofbauer, H.F., Wunnicke, D., Hanelt, I., Hummer, G., and Ernst, R. (2017). Activation of the Unfolded Protein Response by Lipid Bilayer Stress. Mol Cell *67*, 673-684 e678.
Hannun, Y.A. (1996). Functions of Ceramide in Coordinating Cellular Responses to Stress. Science *274*, 1855.
Hannun, Y.A., and Obeid, L.M. (2018). Sphingolipids and their metabolism in physiology and disease. Nat Rev Mol Cell Biol *19*, 175-191.
Hetz, C., Chevet, E., and Harding, H.P. (2013). Targeting the unfolded protein response in disease. Nat Rev Drug Discov *12*, 703-719.
Ho, T.T., Warr, M.R., Adelman, E.R., Lansinger, O.M., Flach, J., Verovskaya, E.V., Figueroa, M.E., and Passegue, E. (2017). Autophagy maintains the metabolism and function of young and old stem cells. Nature *543*, 205-210.
Hotamisligil, G.S. (2017). Inflammation, metaflammation and immunometabolic disorders. Nature *542*, 177-185.
Ito, K., Carracedo, A., Weiss, D., Arai, F., Ala, U., Avigan, D.E., Schafer, Z.T., Evans, R.M., Suda, T., Lee, C.H.*, et al.* (2012). A PML-PPAR-delta pathway for fatty acid oxidation regulates hematopoietic stem cell maintenance. Nat Med *18*, 1350-1358.
Ito, K., and Suda, T. (2014). Metabolic requirements for the maintenance of self-renewing stem cells. Nat Rev Mol Cell Biol *15*, 243-256.
Ito, K., Turcotte, R., Cui, J., Zimmerman, S.E., Pinho, S., Mizoguchi, T., Arai, F., Runnels, J.M., Alt, C., Teruya-Feldstein, J.*, et al.* (2016). Self-renewal of a purified Tie2+ hematopoietic stem cell population relies on mitochondrial clearance. Science *354*, 1156.
Juarez, J.G., Harun, N., Thien, M., Welschinger, R., Baraz, R., Pena, A.D., Pitson, S.M., Rettig, M., DiPersio, J.F., Bradstock, K.F.*, et al.* (2012). Sphingosine-1-phosphate facilitates trafficking of hematopoietic stem cells and their mobilization by CXCR4 antagonists in mice. Blood *119*, 707-716.

Kasai, S., Yamazaki, H., Tanji, K., Engler, M.J., Matsumiya, T., and Itoh, K. (2019). Role of the ISR-ATF4 pathway and its cross talk with Nrf2 in mitochondrial quality control. J Clin Biochem Nutr *64*, 1-12.
Kaufmann, K.B., Garcia-Prat, L., Liu, Q., Ng, S.W.K., Takayanagi, S.-I., Mitchell, A., Wienholds, E., van Galen, P., Cumbaa, C.A., Tsay, M.J., *et al.* (2019). A stemness screen reveals C3orf54/INKA1as a promoter of human leukemia stem cell latency. Blood *133*, 2198.
Kiernan, J., Damien, P., Monaghan, M., Shorr, R., McIntyre, L., Fergusson, D., Tinmouth, A., and Allan, D. (2016). Clinical Studies of Ex Vivo Expansion to Accelerate Engraftment After Umbilical Cord Blood Transplantation: A Systematic Review. Transfus Med Rev.
Knott, S.R.V., Maceli, A.R., Erard, N., Chang, K., Marran, K., Zhou, X., Gordon, A., Demerdash, El, O., Wagenblast, E., Kim, S., et al. (2014). A computational algorithm to predict shRNA potency. Mol. Cell 56, 796–807.
Koberlin, M.S., Snijder, B., Heinz, L.X., Baumann, C.L., Fauster, A., Vladimer, G.I., Gavin, A.C., and Superti-Furga, G. (2015). A Conserved Circular Network of Coregulated Lipids Modulates Innate Immune Responses. Cell *162*, 170-183.
Kohli, L., and Passegue, E. (2014). Surviving change: the metabolic journey of hematopoietic stem cells. Trends Cell Biol *24*, 479-487.
Lai, W.L., and Wong, N.S. (2008). The PERK/eIF2 alpha signaling pathway of Unfolded Protein Response is essential for N-(4-hydroxyphenyl)retinamide (4HPR)-induced cytotoxicity in cancer cells. Exp Cell Res *314*, 1667-1682.
Laurenti, E., Doulatov, S., Zandi, S., Plumb, I., Chen, J., April, C., Fan, J.B., and Dick, J.E. (2013). The transcriptional architecture of early human hematopoiesis identifies multilevel control of lymphoid commitment. Nat Immunol *14*, 756-763.
Laurenti, E., Frelin, C., Xie, S., Ferrari, R., Dunant, C.F., Zandi, S., Neumann, A., Plumb, I., Doulatov, S., Chen, J.*, et al.* (2015). CDK6 levels regulate quiescence exit in human hematopoietic stem cells. Cell Stem Cell *16*, 302-313.
Lee, J.-M., Govindarajah, V., Goddard, B., Hinge, A., Muench, D.E., Filippi, M.-D., Aronow, B., Cancelas, J.A., Salomonis, N., Grimes, H.L., *et al.* (2018). Obesity alters the long-term fitness of the hematopoietic stem cell compartment through modulation of Gfi1 expression. The Journal of Experimental Medicine *215*, 627.
Leeman, D.S., Hebestreit, K., Ruetz, T., Webb, A.E., McKay, A., Pollina, E.A., Dulken, B.W., Zhao, X., Yeo, R.W., Ho, T.T.*, et al.* (2018). Lysosome activation clears aggregates and enhances quiescent neural stem cell activation during aging. Science *359*, 1277.
Lun, A.T.L., Bach, K., Marioni, J.C. (2016) Pooling across cells to normalize single-cell RNA sequencing data with many zero counts. Genome Biology 17, 75.
Lund, T.C., Boitano, A.E., Delaney, C.S., Shpall, E.J., and Wagner, J.E. (2015). Advances in umbilical cord blood manipulation-from niche to bedside. Nat Rev Clin Oncol *12*, 163-174.
Luo, Y., Li, L., Zou, P., Wang, J., Shao, L., Zhou, D., and Liu, L. (2014). Rapamycin enhances long-term hematopoietic reconstitution of ex vivo expanded mouse hematopoietic stem cells by inhibiting senescence. Transplantation *97*, 20-29.
Massberg, S., Schaerli, P., Knezevic-Maramica, I., Kollnberger, M., Tubo, N., Moseman, E.A., Huff, I.V., Junt, T., Wagers, A.J., Mazo, I.B.*, et al.* (2007). Immunosurveillance by hematopoietic progenitor cells trafficking through blood, lymph, and peripheral tissues. Cell *131*, 994-1008.
Mendoza, A., Breart, B., Ramos-Perez, W.D., Pitt, L.A., Gobert, M., Sunkara, M., Lafaille, J.J., Morris, A.J., and Schwab, S.R. (2012). The transporter Spns2 is required for secretion of lymph but not plasma sphingosine-1-phosphate. Cell Rep *2*, 1104-1110.

Milyavsky, M., Gan, O.I., Trottier, M., Komosa, M., Tabach, O., Notta, F., Lechman, E., Hermans, K.G., Eppert, K., Konovalova, Z.*, et al.* (2010). A distinctive DNA damage response in human hematopoietic stem cells reveals an apoptosis-independent role for p53 in self-renewal. Cell Stem Cell *7*, 186-197.
Mohrin, M., Bourke, E., Alexander, D., Warr, M.R., Barry-Holson, K., Le Beau, M.M., Morrison, C.G., and Passegue, E. (2010). Hematopoietic stem cell quiescence promotes error-prone DNA repair and mutagenesis. Cell Stem Cell *7*, 174-185.
Mohrin, M., Shin, J., Liu, Y., Brown, K., Luo, H., Xi, Y., Haynes, C.M., and Chen, D. (2015). A mitochondrial UPR-mediated metabolic checkpoint regulates hematopoietic stem cell aging. Science *347*, 1374.
Nakada, D., Saunders, T.L., and Morrison, S.J. (2010). Lkb1 regulates cell cycle and energy metabolism in haematopoietic stem cells. Nature *468*, 653-658.
Naveiras, O., Nardi, V., Wenzel, P.L., Hauschka, P.V., Fahey, F., and Daley, G.Q. (2009). Bone-marrow adipocytes as negative regulators of the haematopoietic microenvironment. Nature *460*, 259-263.
Notta, F., Doulatov, S., Laurenti, E., Poeppl, A., Jurisica, I., and Dick, J.E. (2011). Isolation of single human hematopoietic stem cells capable of long-term multilineage engraftment. Science *333*, 218-221.
Notta, F., Zandi, S., Takayama, N., Dobson, S., Gan, O.I., Wilson, G., Kaufmann, K.B., McLeod, J., Laurenti, E., Dunant, C.F.*, et al.* (2016). Distinct routes of lineage development reshape the human blood hierarchy across ontogeny. Science *351*, aab2116.
Rahmaniyan, M., Curley, R.W., Obeid, L.M., Hannun, Y.A., and Kraveka, J.M. (2011). Identification of Dihydroceramide Desaturase as a Direct in Vitro Target for Fenretinide. The Journal of Biological Chemistry *286*, 24754-24764.
Schwab, S.R., Pereira, J.P., Matloubian, M., Xu, Y., Huang, Y., and Cyster, J.G. (2005). Lymphocyte sequestration through S1P lyase inhibition and disruption of S1P gradients. Science *309*, 1735-1739.
Siddique, M.M., Li, Y., Chaurasia, B., Kaddai, V.A., and Summers, S.A. (2015). Dihydroceramides: From Bit Players to Lead Actors. J Biol Chem *290*, 15371-15379.
Siddique, M.M., Li, Y., Wang, L., Ching, J., Mal, M., Ilkayeva, O., Wu, Y.J., Bay, B.H., and Summers, S.A. (2013). Ablation of dihydroceramide desaturase 1, a therapeutic target for the treatment of metabolic diseases, simultaneously stimulates anabolic and catabolic signaling. Mol Cell Biol *33*, 2353-2369.
Signer, R.A., Magee, J.A., Salic, A., and Morrison, S.J. (2014). Haematopoietic stem cells require a highly regulated protein synthesis rate. Nature *509*, 49-54.
Simsek, T., Kocabas, F., Zheng, J., Deberardinis, R.J., Mahmoud, A.I., Olson, E.N., Schneider, J.W., Zhang, C.C., and Sadek, H.A. (2010). The distinct metabolic profile of hematopoietic stem cells reflects their location in a hypoxic niche. Cell Stem Cell *7*, 380-390.
Singh, R., Kaushik, S., Wang, Y., Xiang, Y., Novak, I., Komatsu, M., Tanaka, K., Cuervo, A.M., and Czaja, M.J. (2009). Autophagy regulates lipid metabolism. Nature *458*, 1131-1135.
Takubo, K., Nagamatsu, G., Kobayashi, C.I., Nakamura-Ishizu, A., Kobayashi, H., Ikeda, E., Goda, N., Rahimi, Y., Johnson, R.S., Soga, T.*, et al.* (2013). Regulation of glycolysis by Pdk functions as a metabolic checkpoint for cell cycle quiescence in hematopoietic stem cells. Cell Stem Cell *12*, 49-61.
Tarashansky, A.J., Xue, Y., Quake, S.R., Wang, B. (2019) Self-assembling Manifolds in Single-cell RNA Sequencing Data. Elife *8*, e48994.

Thibault, G., Shui, G., Kim, W., McAlister, G.C., Ismail, N., Gygi, S.P., Wenk, M.R., and Ng, D.T. (2012). The membrane stress response buffers lethal effects of lipid disequilibrium by reprogramming the protein homeostasis network. Mol Cell *48*, 16-27.
Tirosh, I., Izar, B., Prakadan, S.M., Hadsworth, M.H., Treacy, D., Trombetta, J.J., Rotem, A., Rodman, C., Lian, C., Murphy, G., et al. (2016) Dissecting the multicellular ecosystem of metastatic melanoma by single-cell RNA-seq. Science 352, 6282.
Turpin, S.M., Nicholls, H.T., Willmes, D.M., Mourier, A., Brodesser, S., Wunderlich, C.M., Mauer, J., Xu, E., Hammerschmidt, P., Bronneke, H.S., *et al*. (2014). Obesity-induced CerS6-dependent C16:0 ceramide production promotes weight gain and glucose intolerance. Cell Metab *20*, 678-686.
van Galen, P., Kreso, A., Mbong, N., Kent, D.G., Fitzmaurice, T., Chambers, J.E., Xie, S., Laurenti, E., Hermans, K., Eppert, K.*, et al.* (2014). The unfolded protein response governs integrity of the haematopoietic stem-cell pool during stress. Nature *510*, 268-272.
van Galen, P., Mbong, N., Kreso, A., Schoof, E.M., Wagenblast, E., Ng, S.W.K., Krivdova, G., Jin, L., Nakauchi, H., and Dick, J.E. (2018). Integrated Stress Response Activity Marks Stem Cells in Normal Hematopoiesis and Leukemia. Cell Reports.
Velten, L., Haas, S.F., Raffel, S., Blaszkiewicz, S., Islam, S., Hennig, B.P., Hirche, C., Lutz, C., Buss, E.C., Nowak, D., *et al*. (2017). Human haematopoietic stem cell lineage commitment is a continuous process. Nature Cell Biology *19*, 271-281.
van Meer, G., and de Kroon, A.I. (2011). Lipid map of the mammalian cell. J Cell Sci *124*, 5-8.
Vu, T.M., Ishizu, A.N., Foo, J.C., Toh, X.R., Zhang, F., Whee, D.M., Torta, F., Cazenave-Gassiot, A., Matsumura, T., Kim, S.*, et al.* (2017). Mfsd2b is essential for the sphingosine-1-phosphate export in erythrocytes and platelets. Nature *550*, 524-528.
Wang, Y.-H., Israelsen, William J., Lee, D., Yu, Vionnie W.C., Jeanson, Nathaniel T., Clish, Clary B., Cantley, Lewis C., Vander Heiden, Matthew G., and Scadden, David T. (2014). Cell-State-Specific Metabolic Dependency in Hematopoiesis and Leukemogenesis. Cell *158*, 1309-1323.
Warr, M.R., Binnewies, M., Flach, J., Reynaud, D., Garg, T., Malhotra, R., Debnath, J., and Passegue, E. (2013). FOXO3A directs a protective autophagy program in haematopoietic stem cells. Nature *494*, 323-327.
Wilkinson, A.C., and Göttgens, B. (2013). Transcriptional Regulation of Haematopoietic Stem Cells. In Transcriptional and Translational Regulation of Stem Cells, G. Hime, and H. Abud, eds. (Dordrecht: Springer Netherlands), pp. 187-212.
Wolf, F.A., Angerer, P., Theis, F.J. (2018) SCANPY: large-scale single-cell gene expression data analysis. Genome Biology 19, 15.
Zheng, W., Kollmeyer, J., Symolon, H., Momin, A., Munter, E., Wang, E., Kelly, S., Allegood, J.C., Liu, Y., Peng, Q.*, et al.* (2006). Ceramides and other bioactive sphingolipid backbones in health and disease: lipidomic analysis, metabolism and roles in membrane structure, dynamics, signaling and autophagy. Biochim Biophys Acta *1758*, 1864-1884.
Zhou, B.O., Yu, H., Yue, R., Zhao, Z., Rios, J.J., Naveiras, O., and Morrison, S.J. (2017). Bone marrow adipocytes promote the regeneration of stem cells and haematopoiesis by secreting SCF. Nature Cell Biology *19*, 891.
Zyryanova, A.F., Weis, F., Faille, A., Alard, A.A., Crespillo-Casado, A., Sekine, Y., Harding, H.P., Allen, F., Parts, L., Fromont, C., *et al*. (2018). Binding of ISRIB reveals a regulatory site in the nucleotide exchange factor eIF2B. Science *359*, 1533.

KEY RESOURCES TABLE

REAGENT or RESOURCE	SOURCE	IDENTIFIER
Antibodies		
FITC–anti-CD45RA	BD	555488
PE–anti-CD90	BD	555596
PECy5–anti-CD49f	BD	551129
V450–anti-CD7	BD	642916
PECy7–anti-CD38	BD	335790
APC–anti-CD10	BD	340923
APCCy7–anti-CD34	BD	custom made by BD
BV711-CD19	BD	563036
Alexafluor700–anti-CD7	BD	561603
Alexafluor700–anti-CD10	BD	563500
BV510-CD45	BD	563891
biotin-Flt3L	BD	
streptavidin-Qdot605	ThermoFisher	Q10101MP
V450-anti-CD15	BD	642917
PE-Cy7-anti-GlyA	Beckman Coulter	PN A71564
PECy5–anti-CD14	Beckman Coulter	PN A22331
FITC-anti-CD3	BD	349201
V500-anti-CD45	BD	560777
PE–anti-CD19	BD	349209
PE–anti-GlyA	Beckman Coulter	A07792
BV786–anti-CD33	BD	740974
PECy5–anti-CD45	Beckman Coulter	A07785
PECy7–anti-CD14	Beckman Coulter	A22331
APC–anti-CD33	BD	551378
APC–anti-CD45	BD	340943
FITC–anti-CD45	BD	347463
V421–anti-CD10	BD	562902
Ki67-PE	BD	556027
Anti-LC3II	NanoTools	5F10
Anti- pEIF2S1	Abcam	ab196460
Goat Anti-mouse secondary antibody Alexa 488	ThermoFisher	A32723
Bacterial and Virus Strains		
Biological Samples		
Human humbilical cord blood samples	Trillium and Credit Valley Hospital	
Mobilized Peripheral Blood	Princess Margaret Cancer Centre	
Chemicals, Peptides, and Recombinant Proteins		
DNase I	Roche	11284932001
Ammonium Chloride	Stem Cell Technologies	07850
AmpliTaq Gold 360 Polymerase	ThermoFisher	4398813

BamH1-HF	NEB	R0136S
Mlu1-HF	Invitrogene	15432-016
FLT3 Ligand	Milteny Biotec	130-096-474
IL6	Milteny Biotec	130-093-934
SCF	Milteny Biotec	130-096-696
TPO	Milteny Biotec	130-095-752
EPO	Janssen	Eprex 10,000 IU/ml
IL-3	Milteny Biotec	130-095-068
GM-CSF	Milteny Biotec	130-093-866
Fenretinide/4HPR	Tocris Biosciences	1396
StemRegenin1	Stem Cell Technologies	72344
UM171	Xcessbio	60223-2
DMSO	Fisher Chemical	D128-500
ATRA	Gift from Gordon Keller	
Bafilomycin A1	Sigma	B1793
ISRIB	Selleckchem	S7400
DAPI	Sigma	10236276001
Critical Commercial Assays		
StemSep™ Human Hematopoietic Progenitor Cell Enrichment Kit	Stem Cell Technologies	14066
CD34 MicroBead Kit, human	Milteny Biotec	130-097-047
LS Columns	Milteny Biotec	130-042-401
Mouse Cell Depletion Kit	Milteny Biotec	130-104-694
SuperScript VILO	ThermoFisher	1754050
Roche Lightcycler 480 using Power SYBR Green	ThermoFisher	4367659
LysoTracker blue	ThermoFisher	L7525
CYTO-ID® Autophagy detection kit	Enzo Life Sciences	ENZ-51031-0050
RNeasy Micro Kit	Qiagen	74004
APC BrdU Flow Kit	BD	552598
CellROX deep red	ThermoFisher	C10422
TMRE	ThermoFisher	T668
RNeasy Plus Micro Kit	Qiagen	74034
Deposited Data		
Index-sorted single cell (sc) RNA-seq data of human HSPCs	Velten et al., 2017	GSE75478
RNA-seq data	Dick lab, Princess Margaret Cancer Centre	GSE125214
RNA-seq data for uncultured LT-HSC, ST-HSC and GMP	Dick lab, Princess Margaret Cancer Centre	GSE125345
Raw RNA-seq data	Dick lab, Princess Margaret Cancer Centre	EGAS00001003756

Experimental Models: Organisms/Strains		
NOD.Cg *Prkdc*scid*Il2rg*tm1Wjl /SzJ	The Jackson Laboratory	005557
Oligonucleotides		
shRNA amplification Forward primer: GGATCCTGTTTGAATGAGGCTTCAGTACTTTACAGA ATCGTTGCCTGCACATCTTGGAAACACTTGCTGGGA TTACTTCT	Kaufmann et. al, 2019	N/A
shRNA amplification Reverse primer: AGTAACGCGTAAAGTGATTTAATTTATACCATTTTAAT TCAGCTTTGTAAAAATGTATCAAAGAGATAGCAAGGT ATTCAGTTTTAGTAAACAAGATAATTGCTCCTAAAGT AGCCCCTTGAAGTCCGAGGCAGTAGGCA	Kaufmann et. al, 2019	N/A
DEGS1 shRNA sequence: TGCTGTTGACAGTGAGCGAGGTCATGAAACTTACTC ATAATAGTGAAGCCACAGATGTATTATGAGTAAGTTT CATGACCCTGCCTACTGCCTCGGA	This paper	N/A
control Renilla shRNA sequence: TGCTGTTGACAGTGAGCGCAGGAATTATAATGCTTA TCTATAGTGAAGCCACAGATGTATAGATAAGCATTAT AATTCCTATGCCTACTGCCTCGGA	This paper	N/A
DEGS1 forward pPCR primer: CAAACATTCCAAACCAGCGAT	This paper	N/A
DEGS1 reverse pPCR primer: GCAGTTGCATTAACCACTCAA	This paper	N/A
GAPDH forward pPCR primer: ACATCGCTCAGACACCATG	This paper	N/A
GAPDH reverse pPCR primer: TGTAGTTGAGGTCAATGAAGGG	This paper	N/A
Recombinant DNA		
shRenilla	Kaufmann et. al, 2019	pLBC2 lentiviral vector
shDEGS1	This manuscript	pLBC2 lentiviral vector
Software and Algorithms		
FACSDiva	BD	
FlowJo v 9.96	Flowjo, LLC	
Prism 7	Graphpad Software	
Extreme Limiting Dilution Analysis (ELDA)	Hu and Smyth, 2009	http://bioinf.wehi.edu.au/software/elda/
GSEA		http://software.broadinstitute.org/gsea/index.jsp
Pathway database, Bader lab (version April 2017)	http://baderlab.org/GeneSets	
Scran	Lun et al., 2016	https://bioconductor.org/packages/release/bioc/html/scran.html
Scanpy	Wolf et al., 2018	https://github.com/theislab/scanpy

Self Assembling Manifold Algorithm	Tarashansky et al., 2018	https://github.com/atarashansky/self-assembling-manifold
Other		
X-Vivo medium	Lonza	04-380Q
Fetal bovine serum	Sigma	F1051-500mL
Iscove's modified Dulbecco's medium (IMDM)	Gibco	12440-053
MethoCult™ Optimum	Stem Cell Technologies	H4034
StemPro™-34 SFM	Gibco	10640-019
StemPro nutrients	Gibco	10641-025
L-glutamine	Multicell	609-065-EL
Pen/Strep	Gibco	15140-122
Human LDL	Stem Cell Technologies	02698

Figure 1

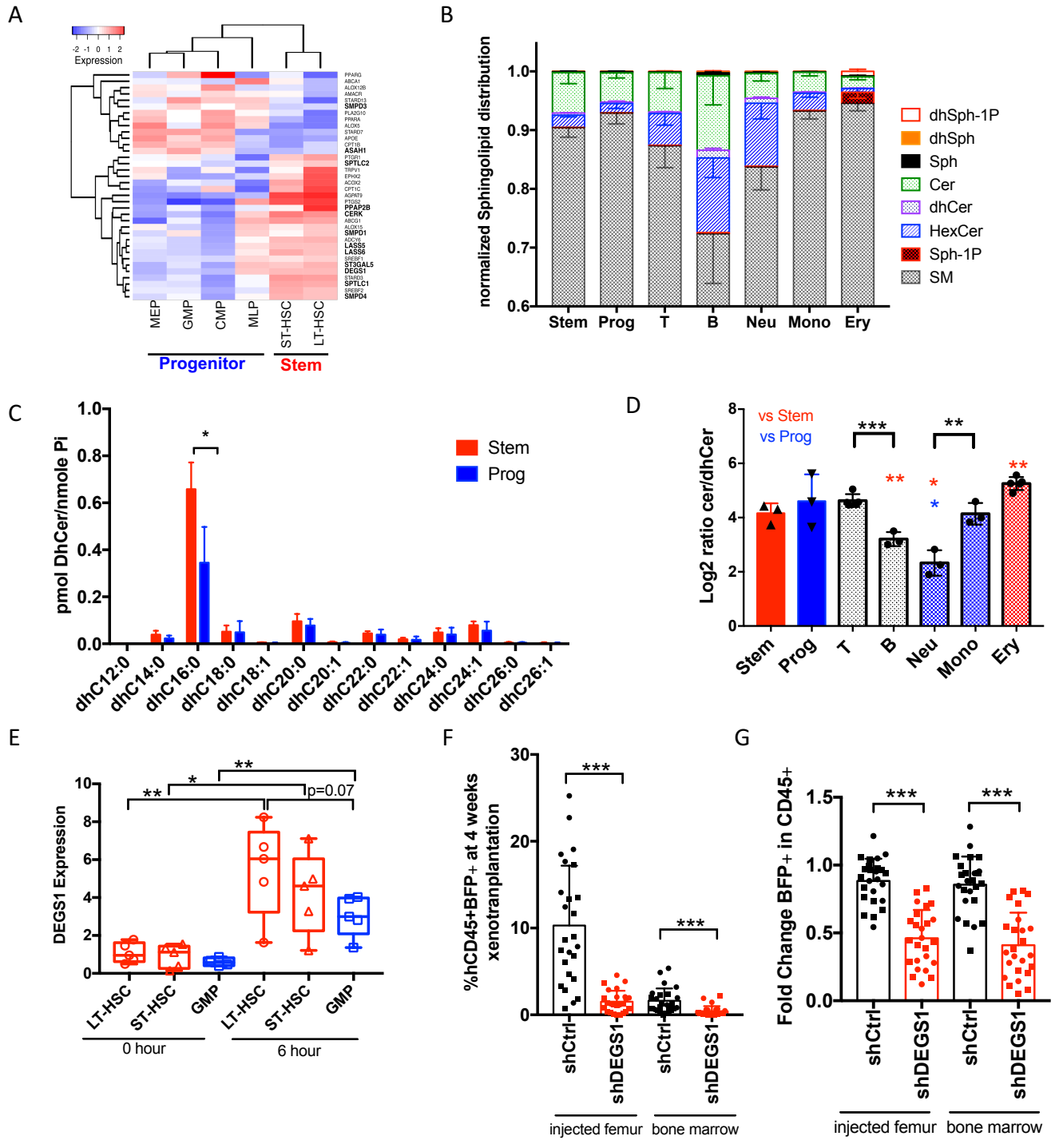
A
Expression
MEP
GMP
CMP
MLP
ST-HSC
LT-HSC
Progenitor
Stem
B
normalized Sphingolipid distribution
Stem
Prog
T
B
Neu
Mono
Ery
dhSph-1P
dhSph
Sph
Cer
dhCer
HexCer
Sph-1P
SM
C
pmol DhCer/nmole Pi
Stem
Prog
dhC12:0
dhC14:0
dhC16:0
dhC18:0
dhC18:1
dhC20:0
dhC20:1
dhC22:0
dhC22:1
dhC24:0
dhC24:1
dhC26:0
dhC26:1
D
Log2 ratio cer/dhCer
vs Stem
vs Prog
E
DEGS1 Expression
p=0.07
LT-HSC
ST-HSC
GMP
0 hour
6 hour
F
%hCD45+BFP+ at 4 weeks xenotranplantation
shCtrl
shDEGS1
injected femur
bone marrow
G
Fold Change BFP+ in CD45+
shCtrl
shDEGS1
injected femur
bone marrow

Figure 2

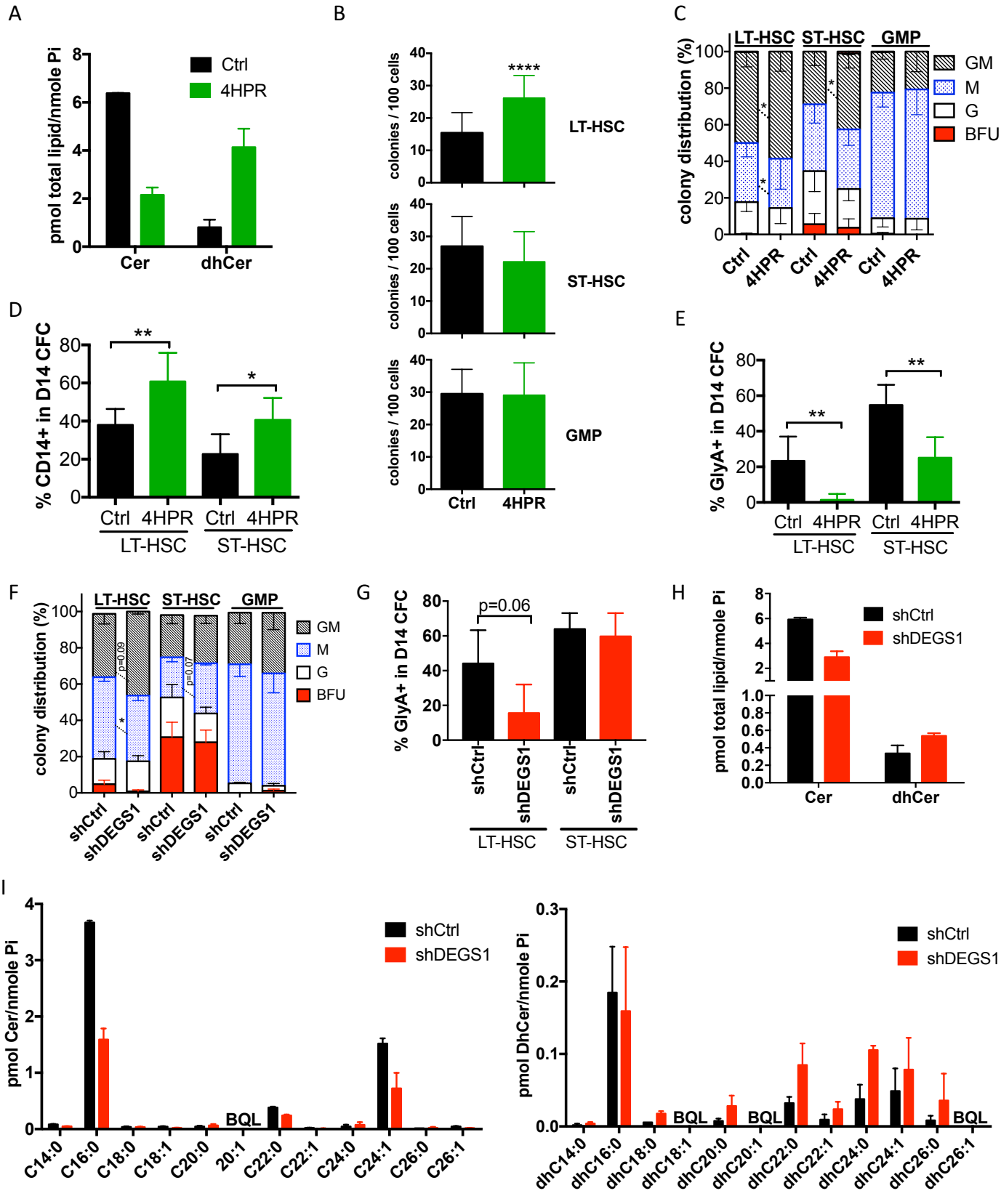
A
pmol total lipid/nmole Pi
Ctrl
4HPR
Cer
dhCer
B
colonies / 100 cells
****
LT-HSC
ST-HSC
GMP
Ctrl
4HPR
C
colony distribution (%)
LT-HSC
ST-HSC
GMP
GM
M
G
BFU
Ctrl
4HPR
D
% CD14+ in D14 CFC
**
*
Ctrl
4HPR
LT-HSC
ST-HSC
E
% GlyA+ in D14 CFC
**
**
Ctrl
4HPR
LT-HSC
ST-HSC
F
colony distribution (%)
LT-HSC
ST-HSC
GMP
GM
M
G
BFU
p=0.09
p=0.07
shCtrl
shDEGS1
G
% GlyA+ in D14 CFC
p=0.06
shCtrl
shDEGS1
LT-HSC
ST-HSC
H
pmol total lipid/nmole Pi
shCtrl
shDEGS1
Cer
dhCer
I
pmol Cer/nmole Pi
shCtrl
shDEGS1
BQL
C14:0
C16:0
C18:0
C18:1
C20:0
20:1
C22:0
C22:1
C24:0
C24:1
C26:0
C26:1
pmol DhCer/nmole Pi
shCtrl
shDEGS1
BQL
dhC14:0
dhC16:0
dhC18:0
dhC18:1
dhC20:0
dhC20:1
dhC22:0
dhC22:1
dhC24:0
dhC24:1
dhC26:0
dhC26:1

Figure 3

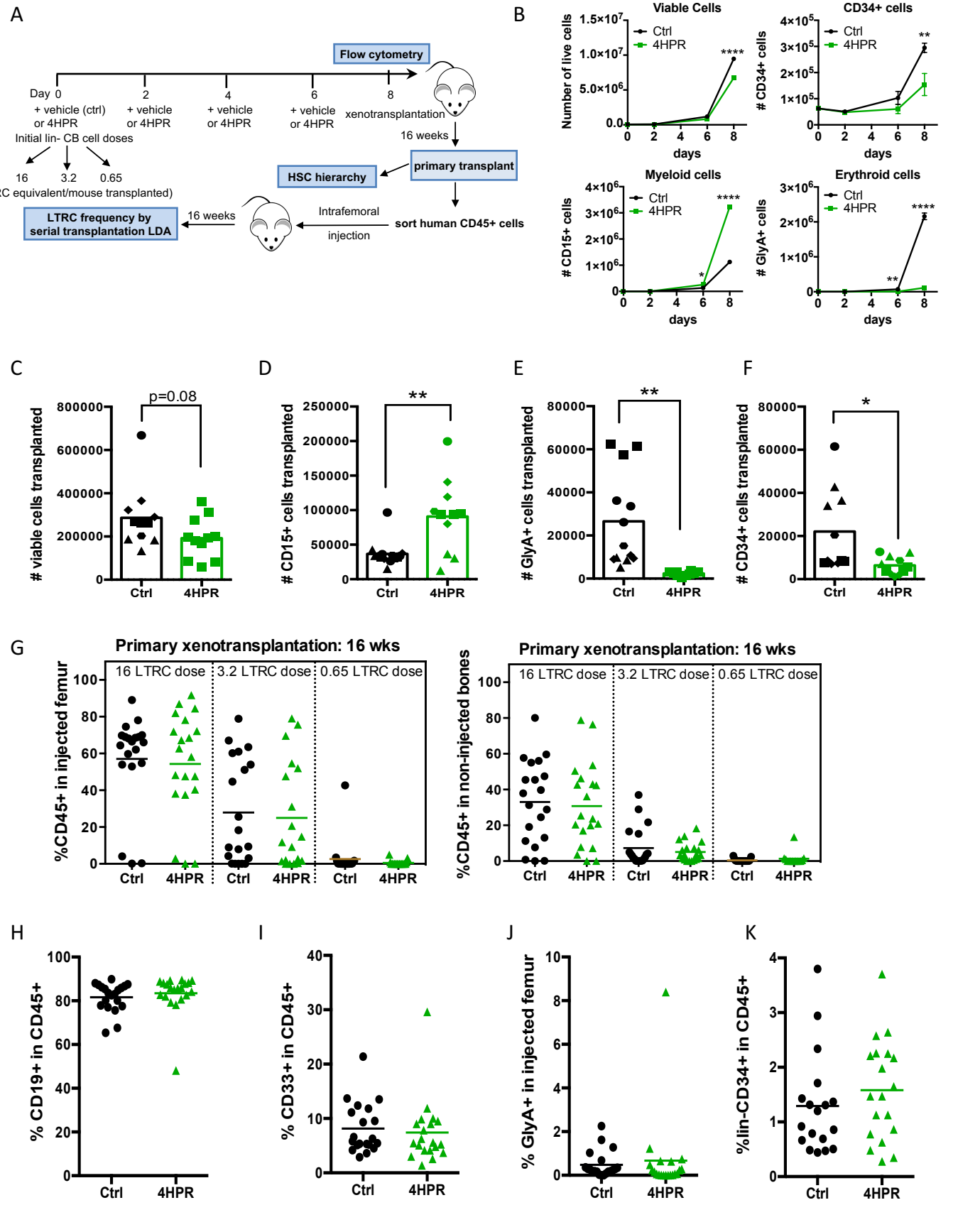
A
Flow cytometry
Day 0
+ vehicle (ctrl) or 4HPR
2
+ vehicle or 4HPR
4
+ vehicle or 4HPR
6
+ vehicle or 4HPR
8
xenotransplantation
Initial lin- CB cell doses
16
3.2
0.65
(LTRC equivalent/mouse transplanted)
16 weeks
primary transplant
HSC hierarchy
sort human CD45+ cells
Intrafemoral injection
16 weeks
LTRC frequency by serial transplantation LDA
B
Viable Cells
Number of live cells
Ctrl
4HPR
days
CD34+ cells
CD34+ cells
Myeloid cells
CD15+ cells
Erythroid cells
GlyA+ cells
C
# viable cells transplanted
p=0.08
D
CD15+ cells transplanted
E
GlyA+ cells transplanted
F
CD34+ cells transplanted
G
Primary xenotransplantation: 16 wks
16 LTRC dose
3.2 LTRC dose
0.65 LTRC dose
%CD45+ in injected femur
%CD45+ in non-injected bones
H
% CD19+ in CD45+
I
% CD33+ in CD45+
J
% GlyA+ in injected femur
K
%lin-CD34+ in CD45+

Figure 4

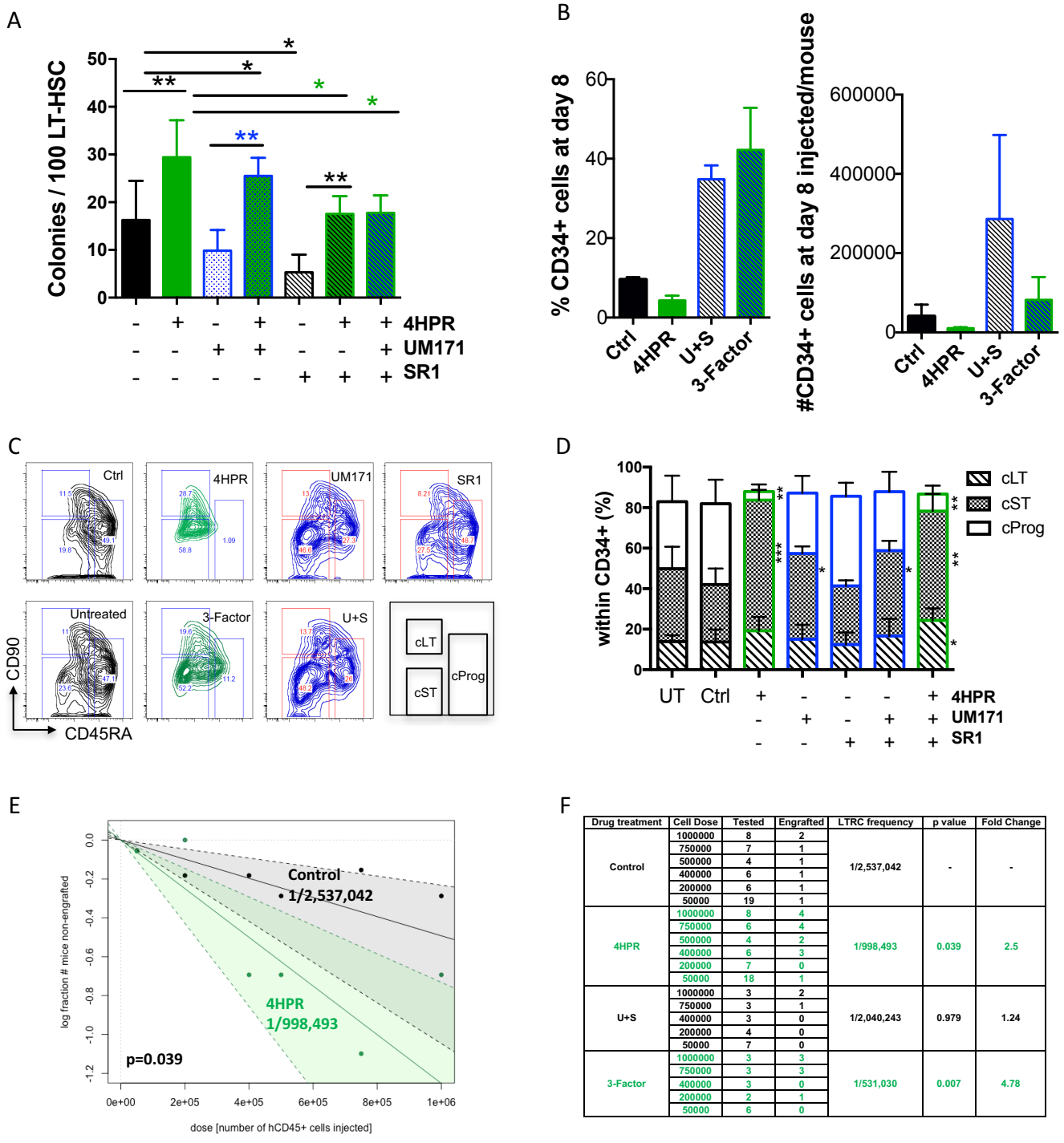

F

Drug treatment	Cell Dose	Tested	Engrafted	LTRC frequency	p value	Fold Change
Control	1000000	8	2	1/2,537,042	-	-
	750000	7	1			
	500000	4	1			
	400000	6	1			
	200000	6	1			
	50000	19	1			
4HPR	1000000	8	4	1/998,493	0.039	2.5
	750000	6	4			
	500000	4	2			
	400000	6	3			
	200000	7	0			
	50000	18	1			
U+S	1000000	3	2	1/2,040,243	0.979	1.24
	750000	3	1			
	400000	3	0			
	200000	4	0			
	50000	7	0			
3-Factor	1000000	3	3	1/531,030	0.007	4.78
	750000	3	3			
	400000	3	0			
	200000	2	1			
	50000	6	0			

Figure 5

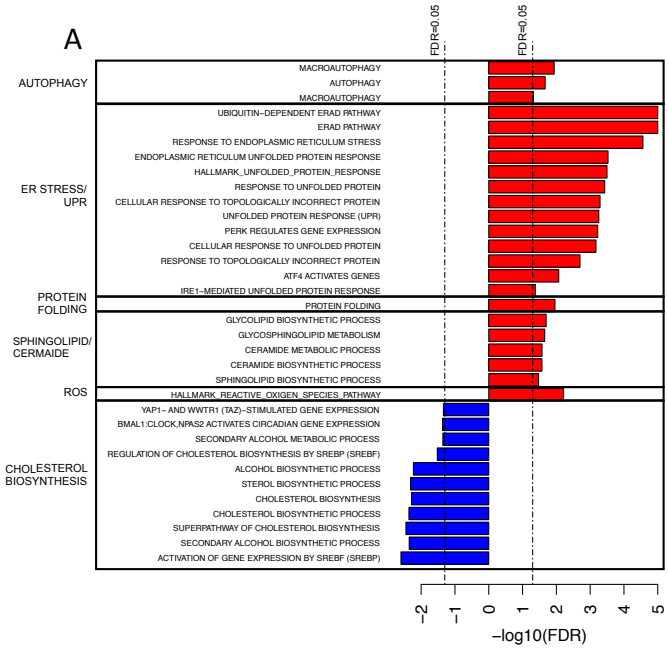
A
FDR=0.05
FDR=0.05
AUTOPHAGY
MACROAUTOPHAGY
AUTOPHAGY
MACROAUTOPHAGY
ER STRESS/ UPR
UBIQUITIN–DEPENDENT ERAD PATHWAY
ERAD PATHWAY
RESPONSE TO ENDOPLASMIC RETICULUM STRESS
ENDOPLASMIC RETICULUM UNFOLDED PROTEIN RESPONSE
HALLMARK_UNFOLDED_PROTEIN_RESPONSE
RESPONSE TO UNFOLDED PROTEIN
CELLULAR RESPONSE TO TOPOLOGICALLY INCORRECT PROTEIN
UNFOLDED PROTEIN RESPONSE (UPR)
PERK REGULATES GENE EXPRESSION
CELLULAR RESPONSE TO UNFOLDED PROTEIN
RESPONSE TO TOPOLOGICALLY INCORRECT PROTEIN
ATF4 ACTIVATES GENES
IRE1–MEDIATED UNFOLDED PROTEIN RESPONSE
PROTEIN FOLDING
PROTEIN FOLDING
SPHINGOLIPID/ CERMAIDE
GLYCOLIPID BIOSYNTHETIC PROCESS
GLYCOSPHINGOLIPID METABOLISM
CERAMIDE METABOLIC PROCESS
CERAMIDE BIOSYNTHETIC PROCESS
SPHINGOLIPID BIOSYNTHETIC PROCESS
ROS
HALLMARK_REACTIVE_OXIGEN_SPECIES_PATHWAY
CHOLESTEROL BIOSYNTHESIS
YAP1– AND WWTR1 (TAZ)–STIMULATED GENE EXPRESSION
BMAL1:CLOCK,NPAS2 ACTIVATES CIRCADIAN GENE EXPRESSION
SECONDARY ALCOHOL METABOLIC PROCESS
REGULATION OF CHOLESTEROL BIOSYNTHESIS BY SREBP (SREBF)
ALCOHOL BIOSYNTHETIC PROCESS
STEROL BIOSYNTHETIC PROCESS
CHOLESTEROL BIOSYNTHESIS
CHOLESTEROL BIOSYNTHETIC PROCESS
SUPERPATHWAY OF CHOLESTEROL BIOSYNTHESIS
SECONDARY ALCOHOL BIOSYNTHETIC PROCESS
ACTIVATION OF GENE EXPRESSION BY SREBP (SREBP)
−2 −1 0 1 2 3 4 5
−log10(FDR)

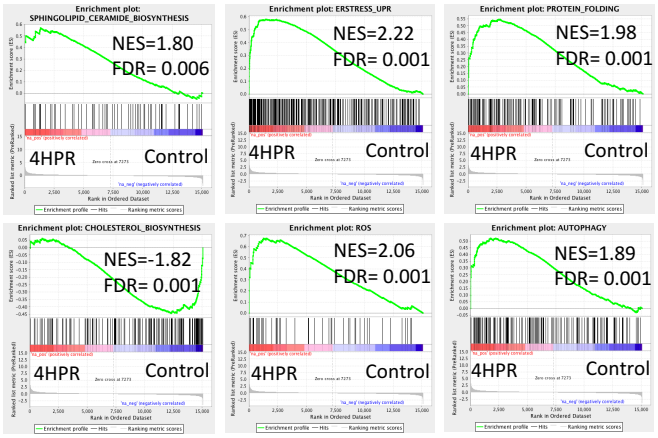
B
Enrichment plot: SPHINGOLIPID_CERAMIDE_BIOSYNTHESIS
NES=1.80
FDR= 0.006
4HPR
Control
Enrichment plot: ERSTRESS_UPR
NES=2.22
FDR= 0.001
4HPR
Control
Enrichment plot: PROTEIN_FOLDING
NES=1.98
FDR= 0.001
4HPR
Control
Enrichment plot: CHOLESTEROL_BIOSYNTHESIS
NES=-1.82
FDR= 0.001
4HPR
Control
Enrichment plot: ROS
NES=2.06
FDR= 0.001
4HPR
Control
Enrichment plot: AUTOPHAGY
NES=1.89
FDR= 0.001
4HPR
Control

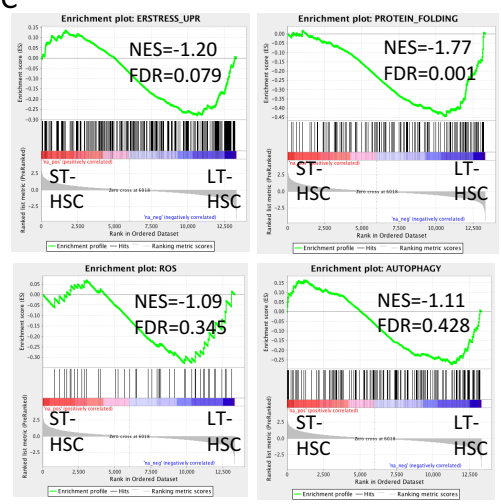
C
Enrichment plot: ERSTRESS_UPR
NES=-1.20
FDR=0.079
ST-HSC
LT-HSC
Enrichment plot: PROTEIN_FOLDING
NES=-1.77
FDR=0.001
ST-HSC
LT-HSC
Enrichment plot: ROS
NES=-1.09
FDR=0.345
ST-HSC
LT-HSC
Enrichment plot: AUTOPHAGY
NES=-1.11
FDR=0.428
ST-HSC
LT-HSC

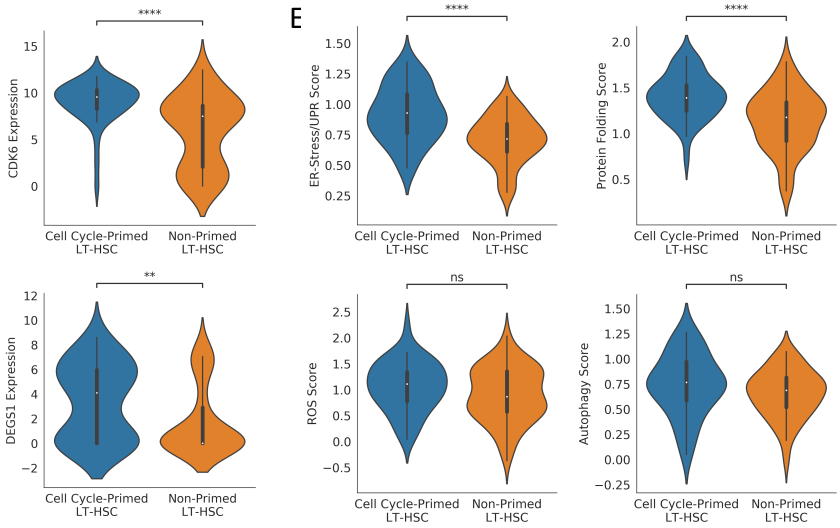
D
CDK6 Expression
DEGS1 Expression
Cell Cycle-Primed LT-HSC
Non-Primed LT-HSC
****
**
E
ER-Stress/UPR Score
Protein Folding Score
ROS Score
Autophagy Score
Cell Cycle-Primed LT-HSC
Non-Primed LT-HSC
****
ns

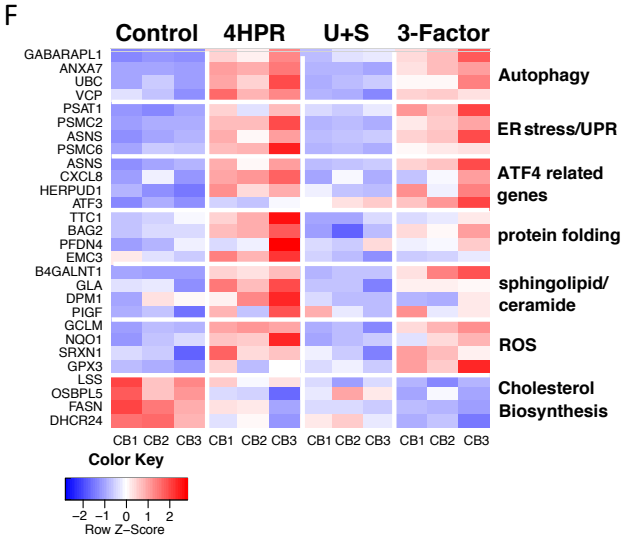
F
Control
4HPR
U+S
3-Factor
GABARAPL1
ANXA7
UBC
VCP
PSAT1
PSMC2
ASNS
PSMC6
ASNS
CXCL8
HERPUD1
ATF3
TTC1
BAG2
PFDN4
EMC3
B4GALNT1
GLA
DPM1
PIGF
GCLM
NQO1
SRXN1
GPX3
LSS
OSBPL5
FASN
DHCR24
Autophagy
ER stress/UPR
ATF4 related genes
protein folding
sphingolipid/ ceramide
ROS
Cholesterol Biosynthesis
CB1 CB2 CB3 CB1 CB2 CB3 CB1 CB2 CB3 CB1 CB2 CB3
Color Key
−2 −1 0 1 2
Row Z−Score

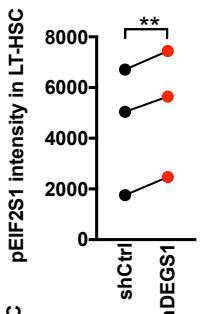
G
pEIF2S1 intensity in LT-HSC
**
shCtrl
shDEGS1

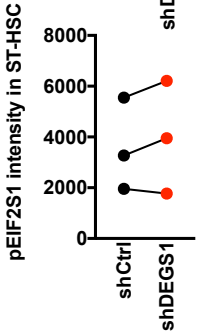
H
pEIF2S1 intensity in ST-HSC
shCtrl
shDEGS1

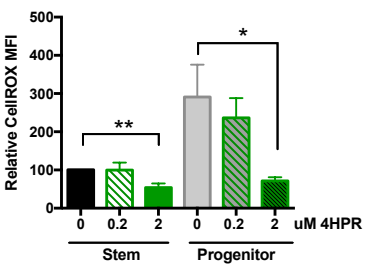
I
Relative CellROX MFI
**
*
0 0.2 2 0 0.2 2 uM 4HPR
Stem
Progenitor

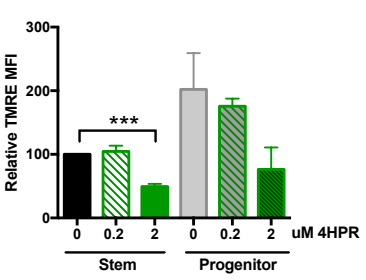
J
Relative TMRE MFI
***
0 0.2 2 0 0.2 2 uM 4HPR
Stem
Progenitor

Figure 6

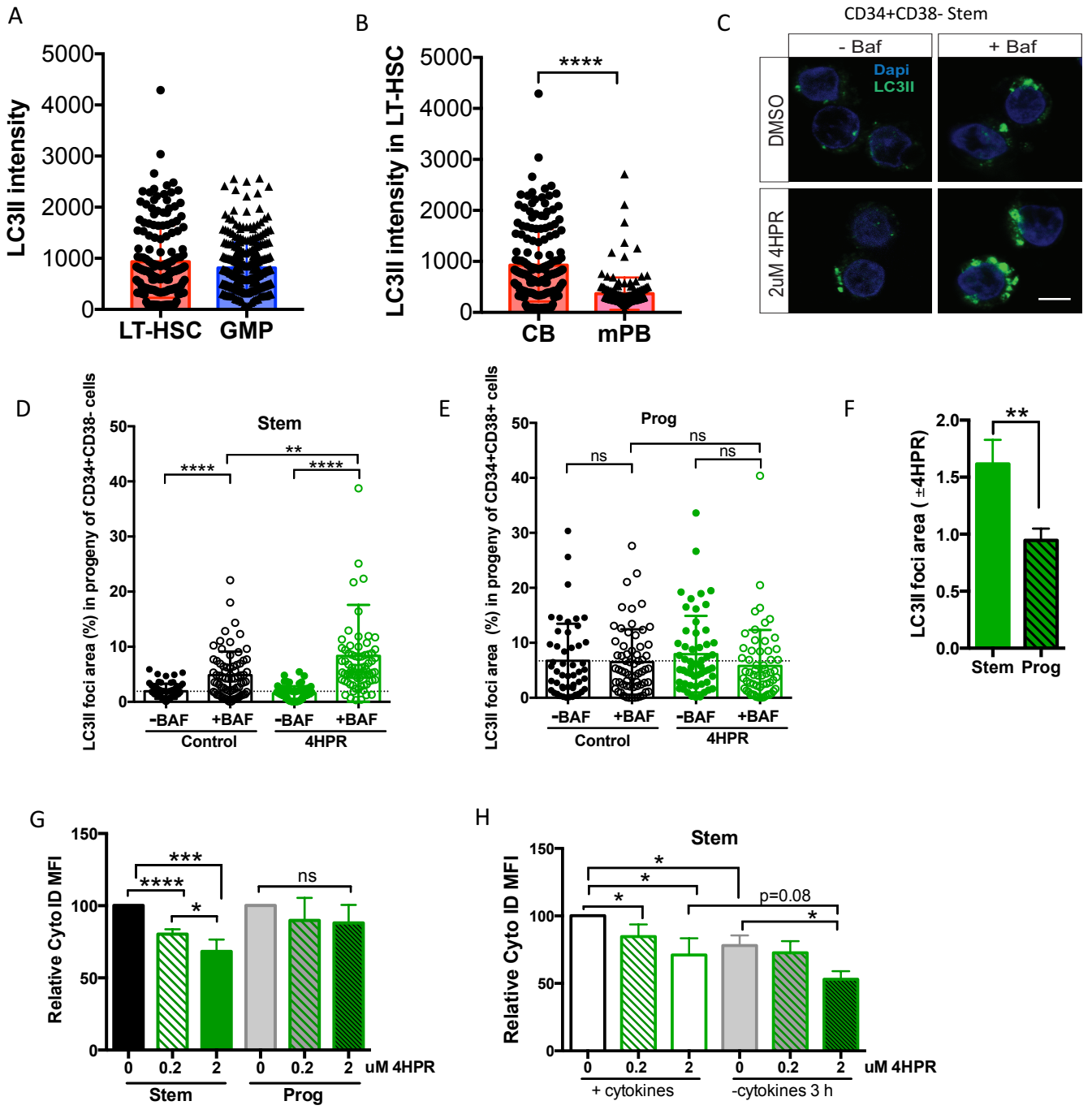
A
LC3II intensity
5000
4000
3000
2000
1000
0
LT-HSC
GMP
B
LC3II intensity in LT-HSC
****
CB
mPB
C
CD34+CD38- Stem
- Baf
+ Baf
Dapi
LC3II
DMSO
2uM 4HPR
D
Stem
LC3II foci area (%) in progeny of CD34+CD38- cells
****
**
****
-BAF
+BAF
-BAF
+BAF
Control
4HPR
E
Prog
LC3II foci area (%) in progeny of CD34+CD38+ cells
ns
ns
ns
F
LC3II foci area (±4HPR)
**
Stem
Prog
G
Relative Cyto ID MFI
***
****
*
ns
0
0.2
2
uM 4HPR
Stem
Prog
H
Stem
Relative Cyto ID MFI
*
*
*
p=0.08
*
+ cytokines
-cytokines 3 h
uM 4HPR

Figure 7

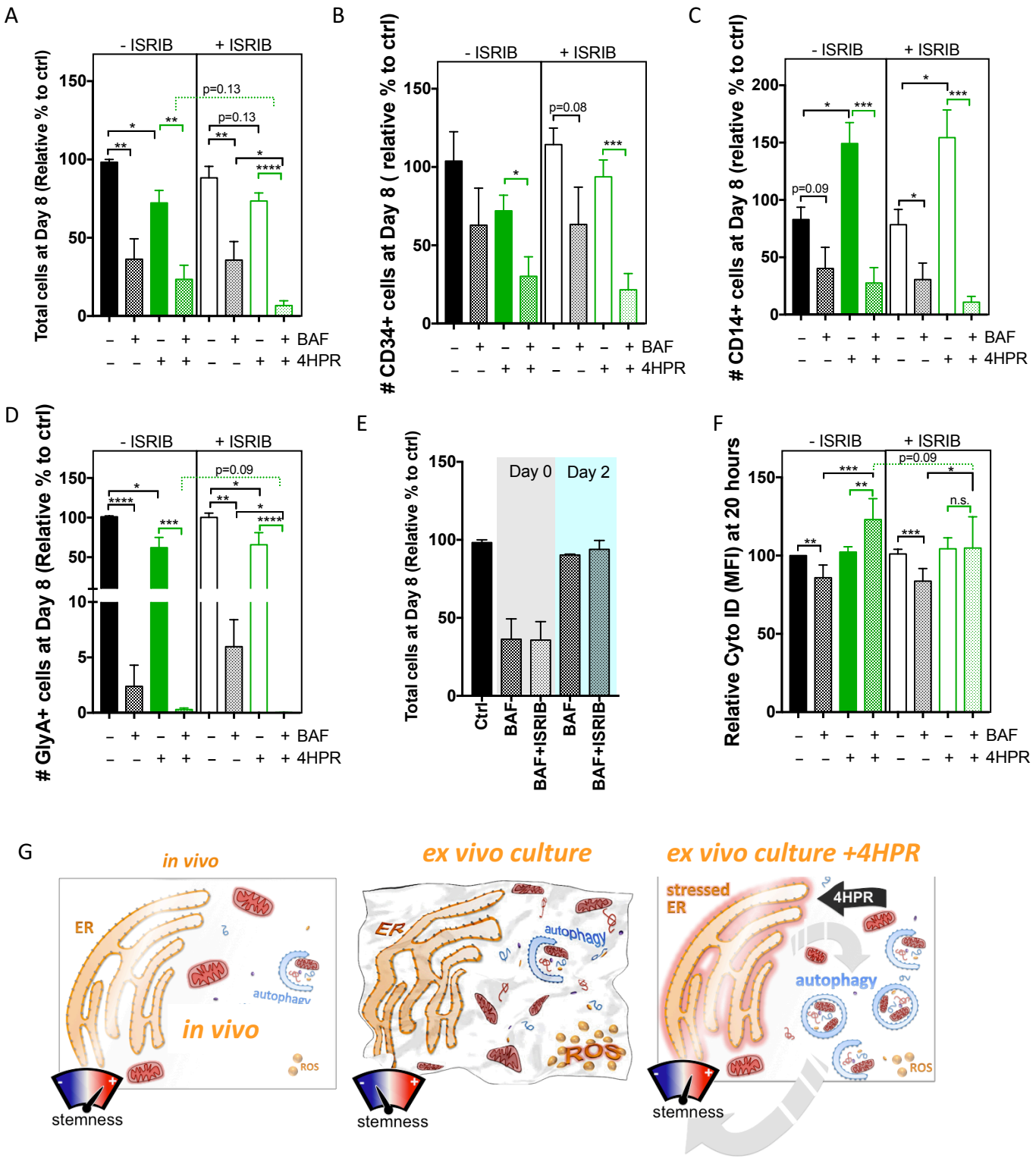
A
- ISRIB
+ ISRIB
Total cells at Day 8 (Relative % to ctrl)
p=0.13
p=0.13
– + – + – + – + BAF
– – + + – – + + 4HPR
B
- ISRIB
+ ISRIB
# CD34+ cells at Day 8 (relative % to ctrl)
p=0.08
– + – + – + – + BAF
– – + + – – + + 4HPR
C
- ISRIB
+ ISRIB
# CD14+ cells at Day 8 (relative % to ctrl)
p=0.09
– + – + – + – + BAF
– – + + – – + + 4HPR
D
- ISRIB
+ ISRIB
# GlyA+ cells at Day 8 (Relative % to ctrl)
p=0.09
– + – + – + – + BAF
– – + + – – + + 4HPR
E
Total cells at Day 8 (Relative % to ctrl)
Day 0
Day 2
Ctrl
BAF
BAF+ISRIB
BAF
BAF+ISRIB
F
- ISRIB
+ ISRIB
Relative Cyto ID (MFI) at 20 hours
p=0.09
n.s.
– + – + – + – + BAF
– – + + – – + + 4HPR
G
in vivo
ER
autophagy
in vivo
ROS
stemness
ex vivo culture
ER
autophagy
ROS
stemness
ex vivo culture +4HPR
stressed ER
4HPR
autophagy
ROS
stemness

Figure S1, related to Figure 1

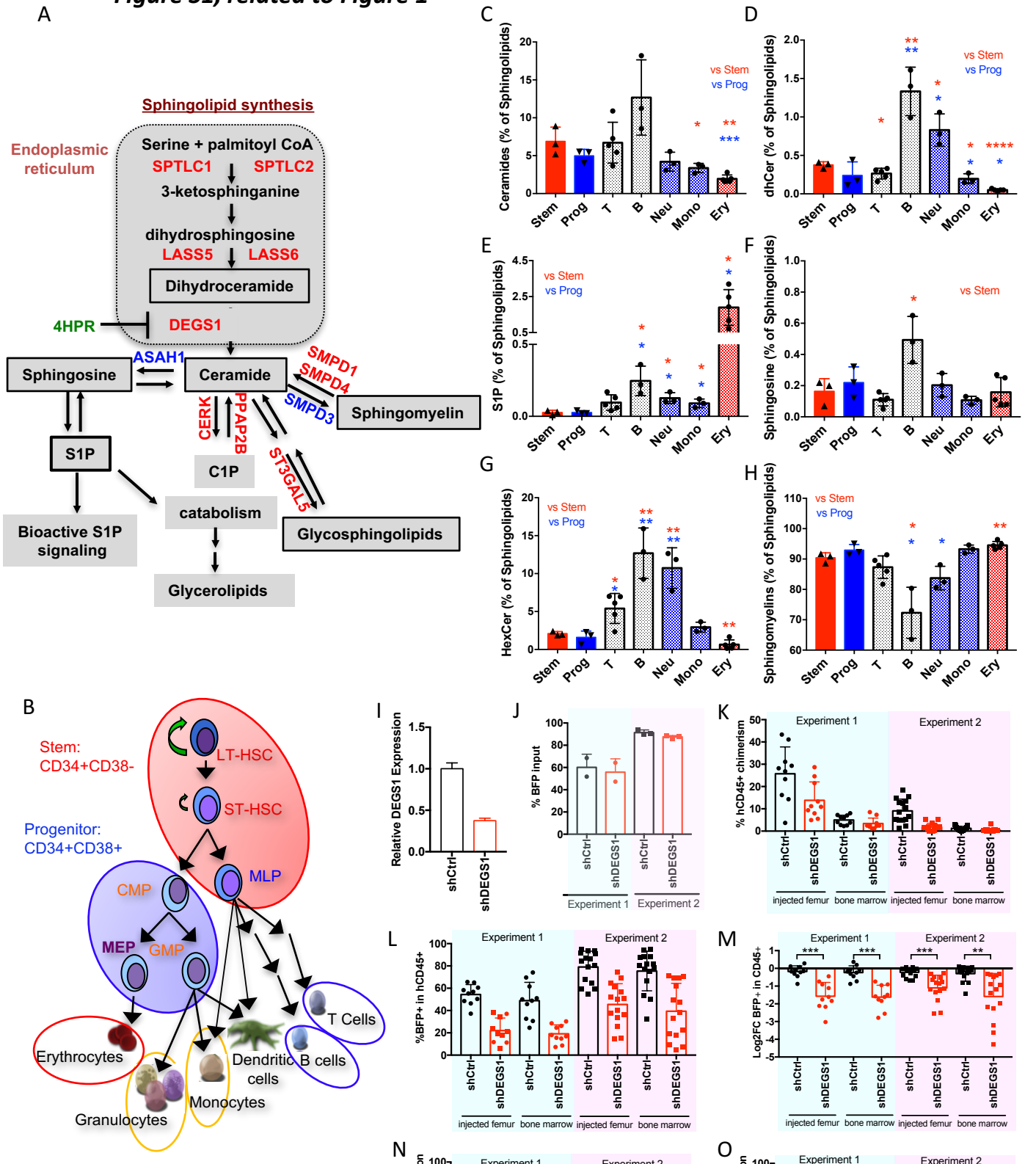

Figure S1, related to Figure 1. DEGS1 contributes to the distinct wiring of sphingolipid synthesis in the human hematopoietic hierarchy and is functionally required *in vivo*. (A) Schematic showing where the SpL genes from Figure 1A lie in the SpL metabolic pathway. Genes more highly expressed in LT-HSC/ST-HSC are in red and genes more highly expressed in committed progenitors are in blue. DEGS1 is a biosynthetic enzyme in *de novo* SpL synthesis, which occurs in the ER, and its activity can be inhibited by 4HPR. (B) Schematic showing the human hematopoietic hierarchy and the 2 HSPC populations and 5 mature populations isolated from CB for measurement of the SpL species indicated in Figure S1A in black boxes by LC/MS. (C) Cer, (D) dhCer, (E) S1P, (F) sphingosine (Sph), (G) hexCer, and (H) SM as percentage of all SpLs measured. (I) KD efficiency of shDEGS1 was quantified in MOLM13 with shCtrl or shDEGS normalized to GAPDH expression. Two separate lentiviral KD experiments in CB $CD34^{+}CD38^{-}$ cells were performed and presented separately (J-O). (J) The transduction input is the % of BFP^{+} cells at 3 days post-transduction for Experiment 1 (n=2 CB pools) and Experiment 2 (n=3 CB pools). Each CB pool was transplanted into 5 individual mice and (K) human $CD45^{+}$ chimerism, (L) % BFP^{+} in $CD45^{+}$ cells, and (M) log2 fold change of BFP^{+} cells ($CD45^{+}$-output vs input), (N) % $CD19^{+}$ cells in BFP^{+} fraction and (O) % $CD33^{+}$ myeloid cells in the BFP^{+} fraction at 4 weeks post-transduction in the injected femur and contra-lateral bones of each mouse was measured by flow cytometry.

Figure S2, related to Figure 2

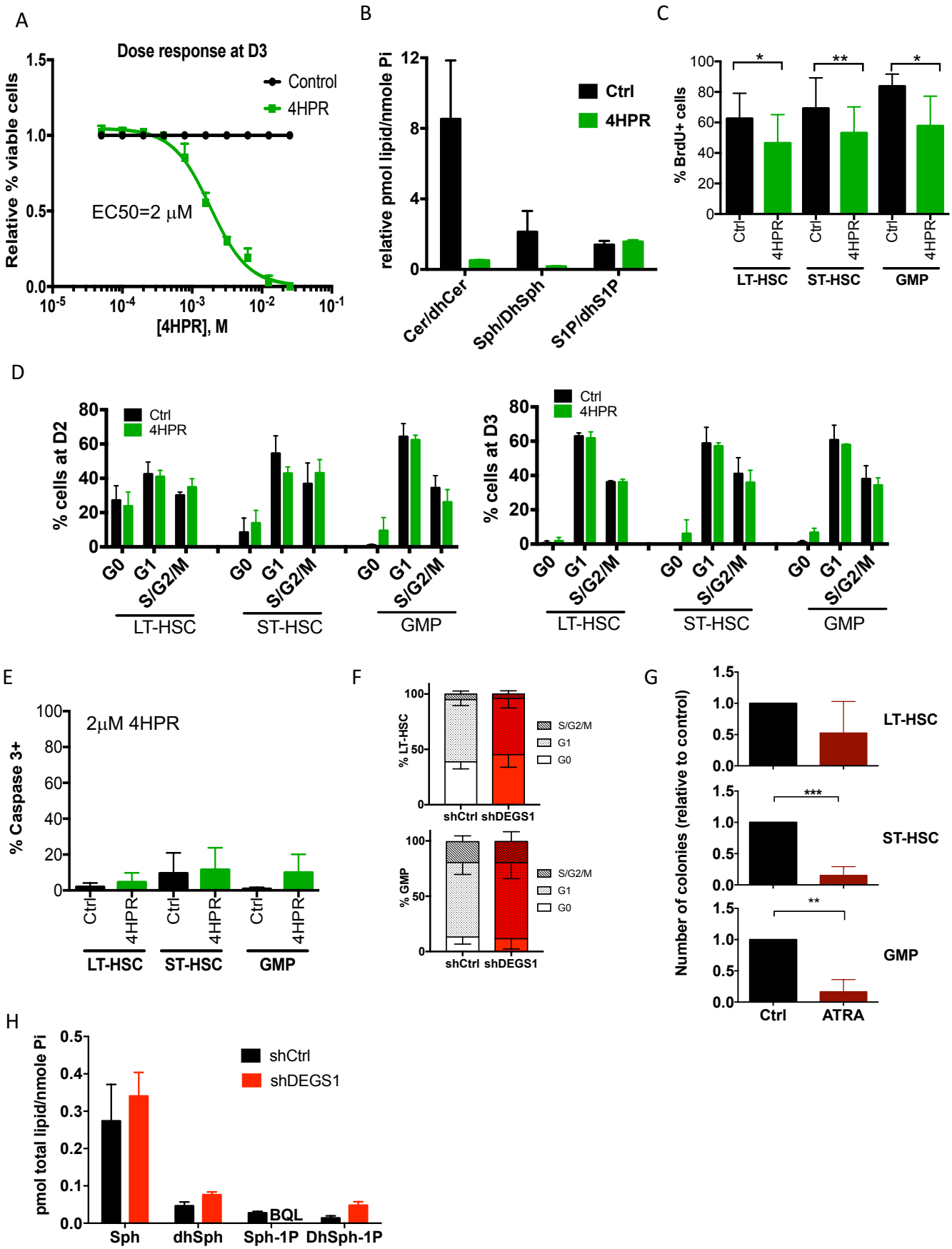

Figure S2, related to Figure 2. Sphingolipid modulation of DEGS1 alters HSC function and lineage balance *in vitro*. (A) Dose response of varying [4HPR] in lin- CB at day 3 post-treatment showing 2uM 4HPR gives the relative half maximal number of viable cells compared to control (n=3). (B) Relative levels of Cer/dhCer, sphingosine (sph)/dihydrosphingosine (dhSph), and S1P/dihydro-S1P (dhS1P) levels in lin- CB cells cultured for 8 days with control or 4HPR (n=2) as measure by lipid LC/MS. The relative levels of lipid/dihydro-lipid show that 4HPR causes accumulation of dhCer and decreases total Cer. However, relative levels of the signaling lipid S1P compared to dhS1P is unchanged by 4HPR treatment compared to control. (C) % BrdU+ cells following 4 or 8 hours labeling at 3d post-treatment with the indicated sorted cell populations shows 4HPR decreases the proliferation rate of primitive CB subpopulations in culture (n=4, paired t-Test). Cell cycle analysis for Ki67 and DNA content by flow cytometry of sorted LT-, ST-HSC, or GMP at (D) day 2 (n=3) or day 3 post treatment (n=2) with vehicle control or 4HPR shows 4HPR does not significantly prevent sorted LT-HSC, ST-HSC or GMP grown in 4HPR from exiting quiescence and transiting through the cell cycle. (E) Flow cytometry for % of cells exhibiting cleaved Caspase 3 with 2uM 4HPR treatment (n=4) at day 3. (F) LT-HSC or GMP purified from 4 week xenografts expressing shCtrl or shDEGS1 by flow cytometry were analyzed for cell cycle distribution with Ki67 and DNA content. (G) Relative colonies formed by LT-HSC, ST-HSC, or GMP treated with $2\ \mu M$ ATRA in CFC assays following 10 days. (H) LC/MS analysis for Sph, dihydrosphingosine (dhSph), Sph-1P and dhSph-1P. Species below quantitation level (BQL) are indicated.

Figure S3, related to Figure 3

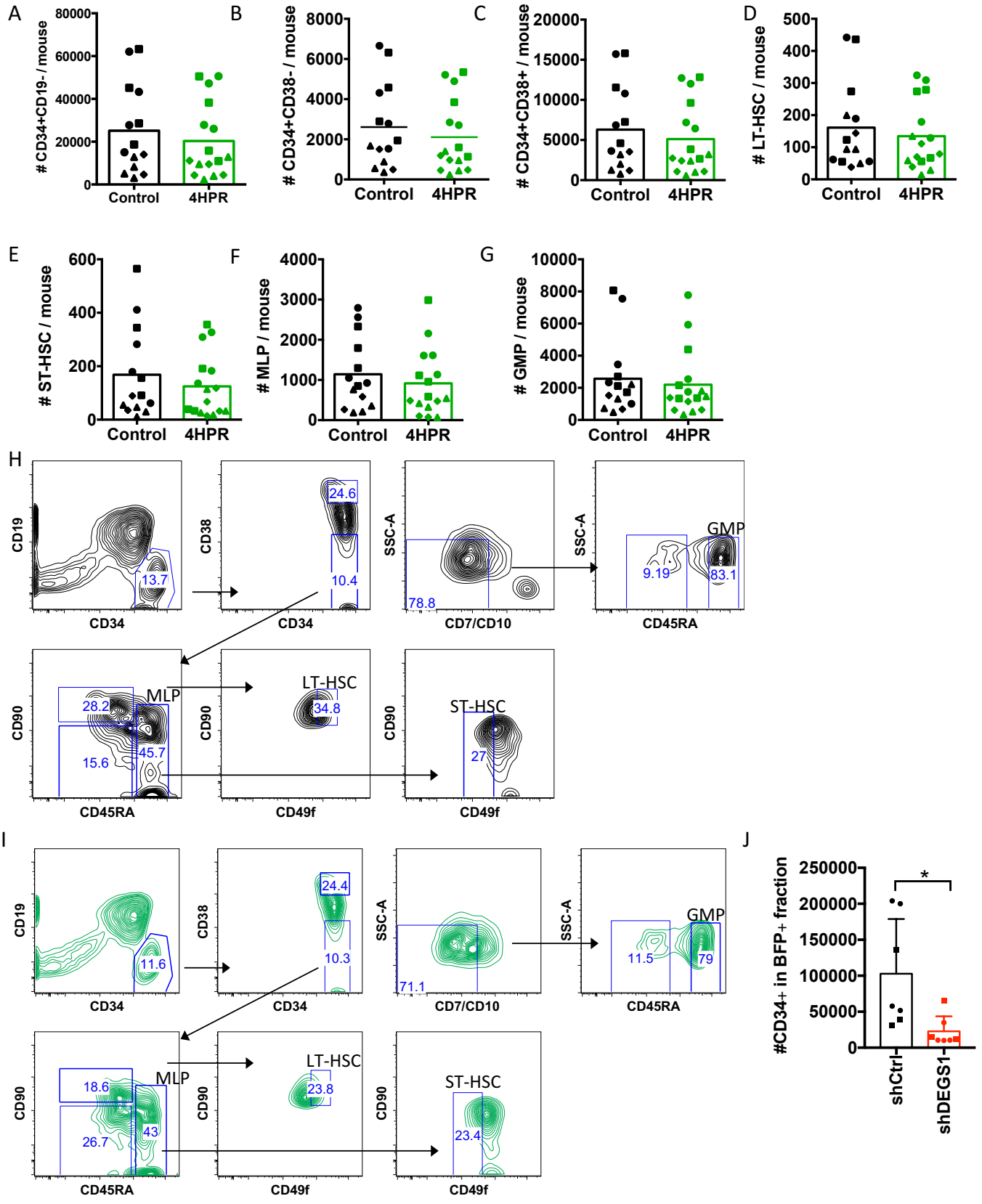

Figure S3, related to Figure 3. *Ex vivo* treatment with 4HPR maintains HSC function following xenotransplantation. (A-I) Flow cytometry analysis were performed on human CD34+ enriched cells following Miltenyi human CD34 enrichment from mice engrafted with control or 4HPR-treated cells at the 16 HSC dose for the human CB hierarchy from 4 biological experiments, marked with different symbols (n=4 mice per biological experiment). The number of (A) CD34+CD19- cells, (B) CD34+CD38-, (C) CD34+CD38+, (D) LT-HSC, (E) ST-HSC, (F) MLP, and (G) GMP were quantitated from each mouse at 16 weeks post-transplant. Representative HSC hierarchy analysis scheme of CD34 enriched cells isolated from mice 16 weeks post-transplantation engrafted with *ex vivo* cultured CB cells in the presence of (H) vehicle control (black) or (I) 4HPR (green). (J) Mice from Figure 1F-G were pooled and analyzed for the number of CD34+ shCtrl or shDEGS1 BFP+ transduced cells in the CD45+ fraction (mice were pooled for CB xenografts, technical duplicates for 2 CB xenografts).

Figure S4, related to Figure 4

A

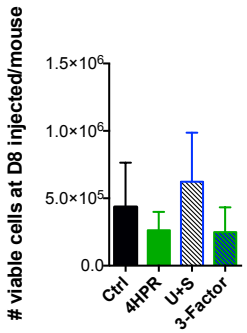

B

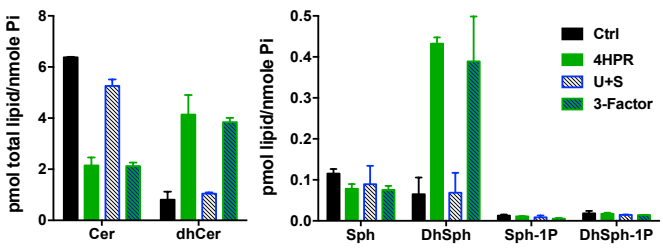

C

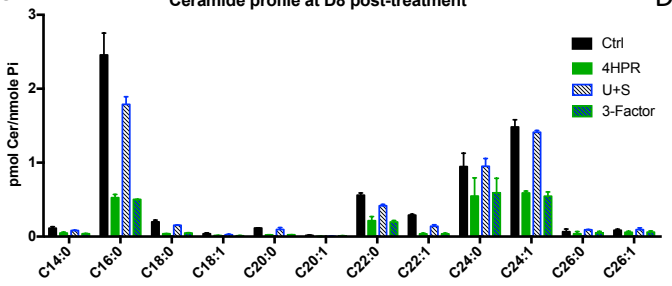

D

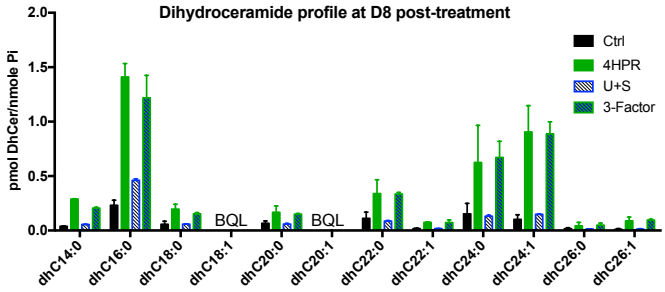

E

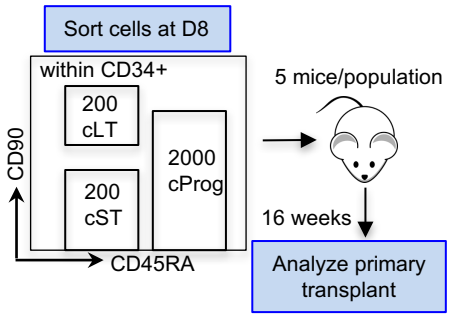

F

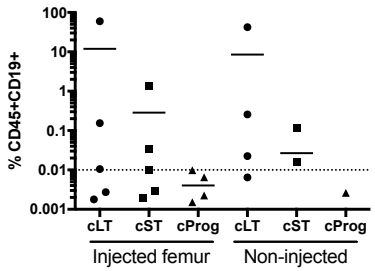

G

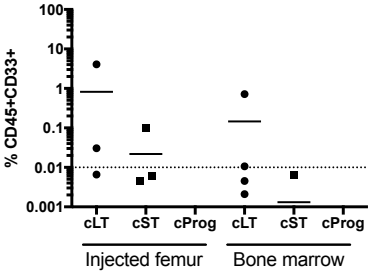

H

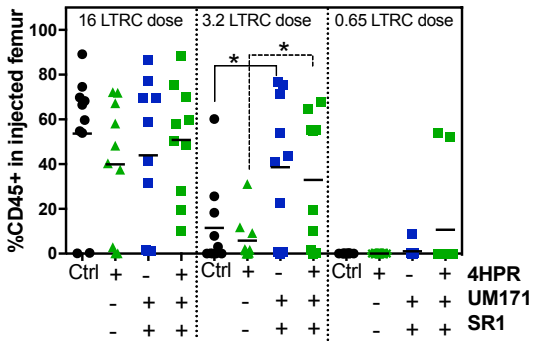

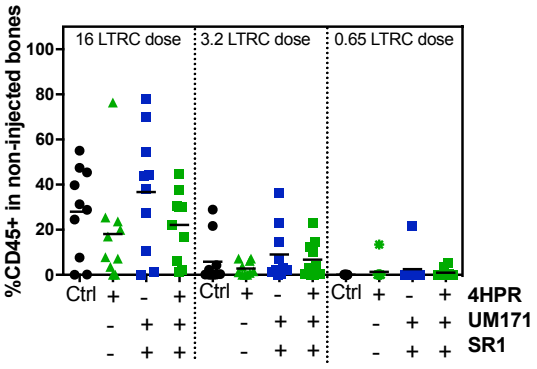

I

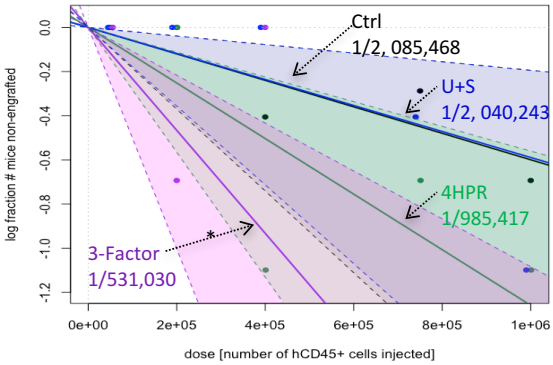

J

Drug treatment	Cell Dose	Tested	Engrafted	LTRC frequency	p value	Fold Change
Control	1000000	2	1	1/2,085,468	-	-
	750000	4	1			
	400000	3	1			
	200000	4	0			
	50000	8	0			
4HPR	1000000	3	2	1/985,417	0.280	2.11
	750000	4	2			
	400000	3	2			
	200000	4	0			
	50000	7	0			
U+S	1000000	3	2	1/2,040,243	0.979	1.02
	750000	3	1			
	400000	3	0			
	200000	4	0			
	50000	7	0			
3-Factor	1000000	3	3	1/531,030	0.043	3.92
	750000	3	3			
	400000	3	0			
	200000	2	1			
	50000	6	0			

Figure S4, related to Figure 4. Sphingolipid modulation with 4HPR restricts expansion of committed progenitors during *ex vivo* culture to enhance HSC self-renewal. (A) The number of cells following 8 days of ex vivo culture at the 16 LTRC dose transplanted per mouse at the indicated drug treatments (n=2). (B) LC/MS analysis for total Cer, dhCer, Sph, dhSph, Sph-1P and dhSph-1P levels show that 4HPR increases dhCer and dhSph alone or in combination with UM171 and SR1 (n=2). (C) The Cer and (D) dhCer profiles normalized to cellular inorganic phosphate levels with the indicated fatty-acyl chain of cells collected following 8 days of culture with indicated treatments. Species below quantitation level (BQL) are indicated. (E) The indicated cell populations were sorted from the CD34+ fraction of lin-CB cultured for 8 days and transplanted into NSG mice to determine human lymphoid and myeloid engraftment. (F) Lymphoid (CD45+CD19+) and (G) myeloid (CD45+CD33+) engraftment from S5A at 16 weeks post-transplantion, Engraftment considered positive at 0.01%. (H) Human CD45 chimerism in the injected femurs and non-injected bones of transplanted mice for the indicated cell doses at 16 weeks xenotransplantion following 8 days *ex vivo* culture with indicated drugs. (I-J) LTRC frequency plot and table from serial transplantation for 2 biological experiments with control, 4HPR, U+S, and 3-Factor treatments were calculated separated and shown.

Figure S5, related to Figure 5 and Table S1,S2 and S3

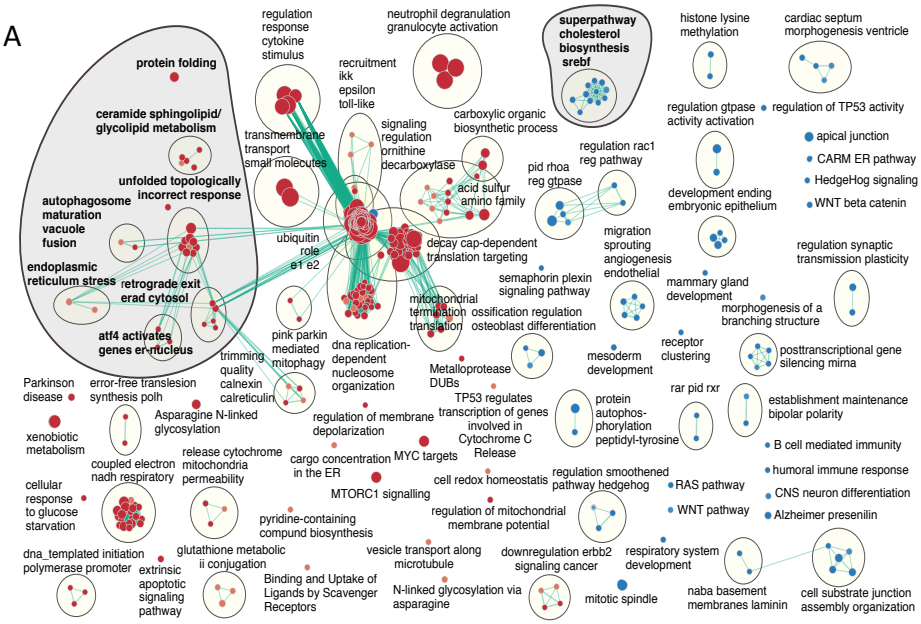

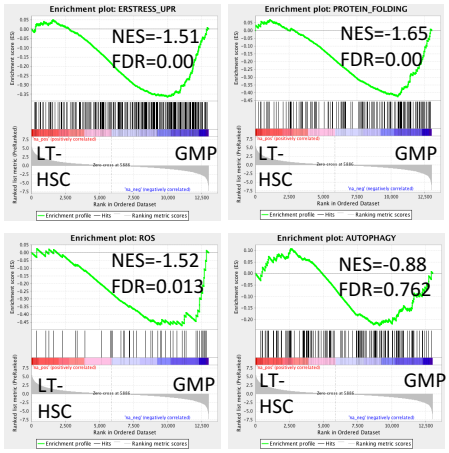

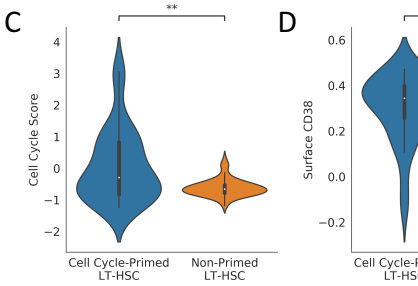

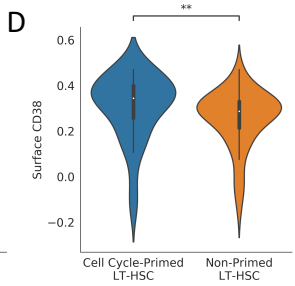

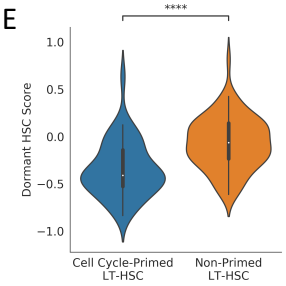

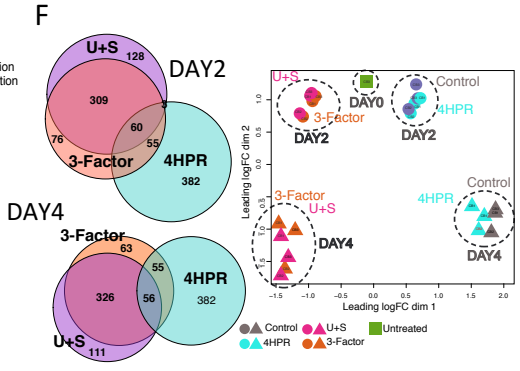

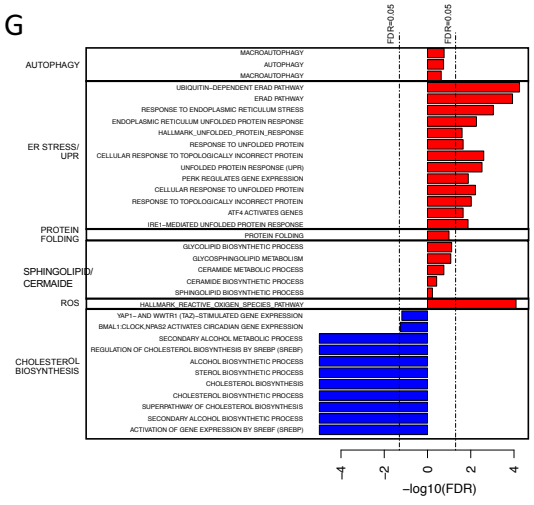

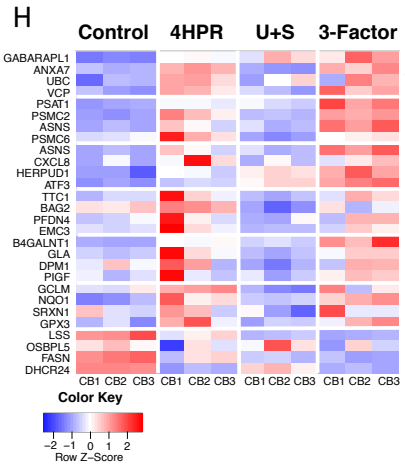

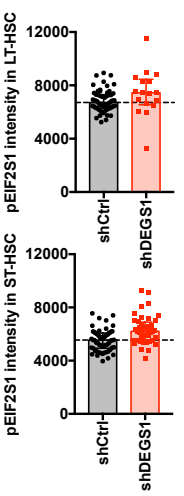

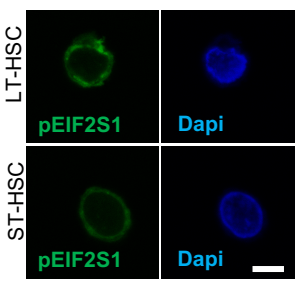

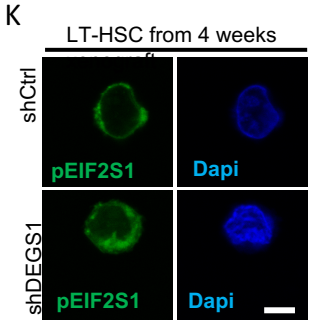

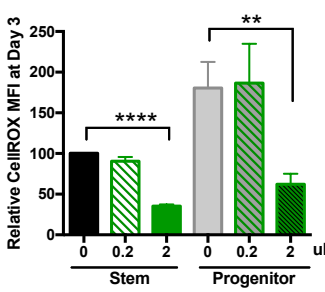

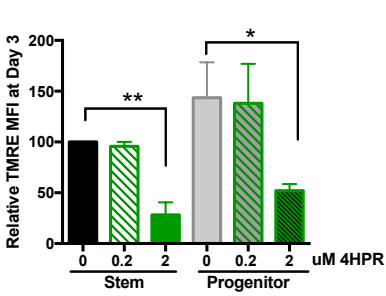

Figure S5, related to Figure 5 and Tables S1, S2 and S3. Sphingolipid modulation with 4HPR treatment upregulates cellular stress pathways and remodels cellular metabolism in HSPC during *ex vivo* culture. (A) Enrichment map at day 2 of 4HPR gene-sets with positive and negative normalized enrichment score (NES) at FDR<0.05 relative to control treatment. Node size is proportional to NES. Red node: positive NES and enrichment in genes up-regulated by 4HPR treatment. Blue node: negative NES and enrichment in genes down-regulated by 4HPR treatment. Green edges indicate gene overlap. (B) GSEA of autophagy, ERstress/UPR, protein folding or ROS pathways in uncultured LT-HSC vs GMP. (C-E) LT-HSC from Velten, et al. were clustered as cell cycle-primed or non-primed as described in methods: (C) cell cycle programs, (D) CD38 surface expression, and (E) dormant HSC programs are shown. significance calculated with Wilcoxon rank sum test for S5C-E, $p<0.05$ (*), $p<0.01$ (**), $p<0.001$(***), $p<0.0001$ (****). (F) Venn-Diagram at day 2 and day 4 showing number of overlap between top 500 up regulated genes in 4HPR, U+S and 3-Factor treatments. Multi Dimension Scaling (MDS) plot (right) showing similarities between samples at day 2 and day 4. Samples with closest distances are circled with dashed lines. (G) NES scores at day 4 for indicated gene sets from Figure 5A with 4HPR treatment relative to control. (H) Heatmap of gene expression at day 4 for the top 4 genes in selected functional modules from Figure 5B upregulated by 4HPR treatment at day 2. (I) pEIF2S1 intensity for individual cells from 1 CB for BFP^+ isolated from 4 week xenografts engrafted with shCtrl or shDEGS1 stem cells. Representative pEIF2S1 confocal microscopy images for (J) shCTRL LT-HSC and shCtrl ST-HSC and (K) shCtrl or shDEGS1 LT-HSC. Flow cytometry analysis for (L) relative CellROX and (M) relative mitochondrial membrane potential with TMRE in the progeny of CD34+CD38- stem or CD34+CD38+ progenitor CB cells at day 2 post-treatment with indicated concentrations of 4HPR.

Figure S6, related to Figure 6

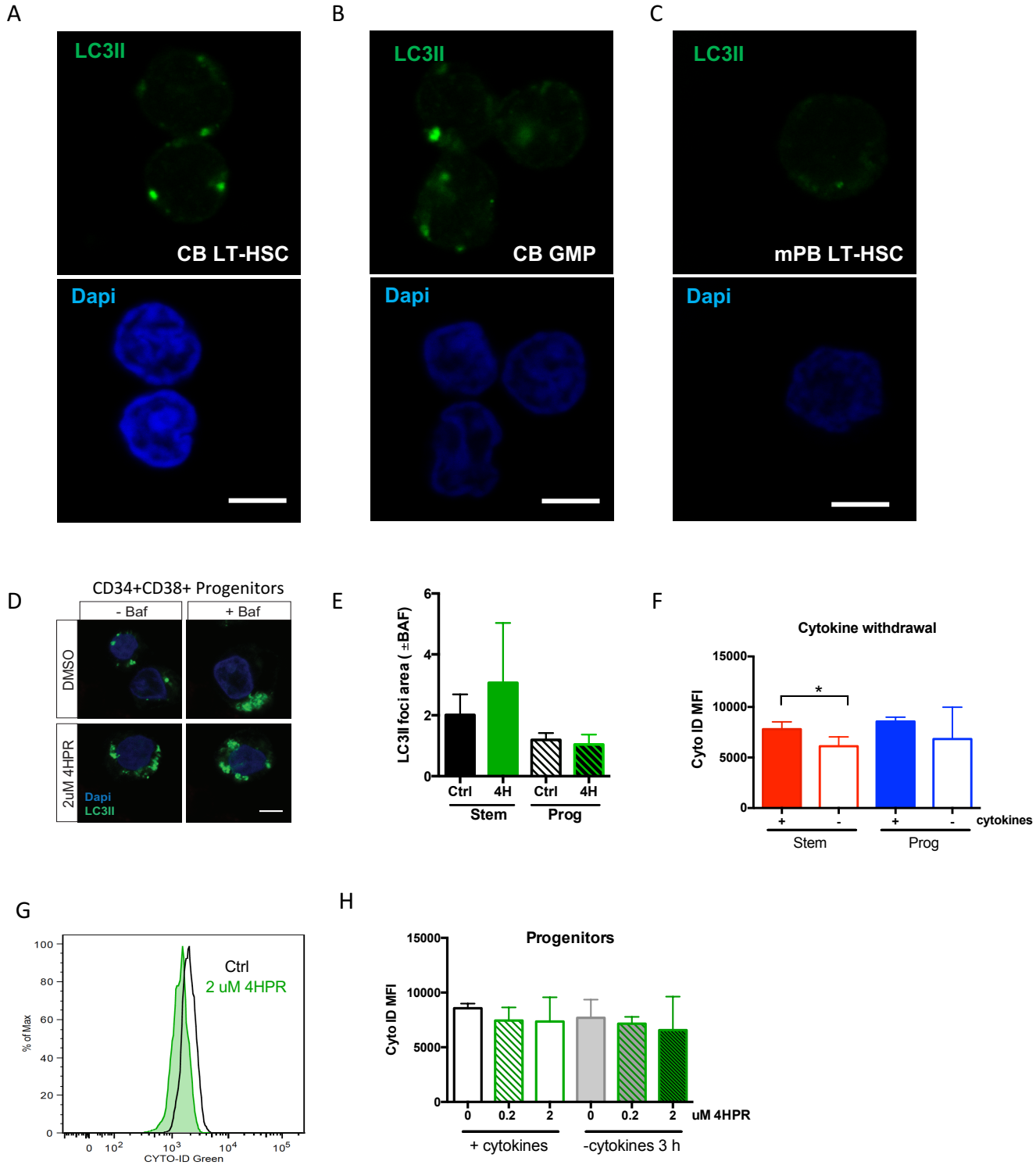

Figure S6, related Figure 6. 4HPR activates autophagy in HSPC during *ex vivo* culture. Representative immunofluorescence images of DAPI (blue) and LC3II staining (green) for uncultured (A) CB LT-HSC, (B) CB GMP, (C) mPB LT-HSC, and (D) CD34+CD38+ cells (prog) following 2 days of treatment with control or 2 μM 4HPR with and without BAF for 12 hours. Scale is 5 μm. (E) Autophagic flux quantification as a ratio of LC3II foci area with and without BAF for Figure 6D-E (n=3). (F) Cyto ID MFI following 3 hours of cytokine withdrawal at 2 days post in vitro culture shows only stem, but not progenitor cells activate autophagic flux upon cytokine withdrawal. (G) Representative flow cytometry histogram plot of Cyto-ID fluorescence intensity of control (black) and 4HPR (green) treated stem cells to assay for autophagic flux. Lower mean fluorescence intensity (MFI) indicates more turnover of autophagosomes and thus increased autophagic flux. (H) CytoID MFI measurements for Figure 3G and the comparable data for progenitor samples to illustrate autophagic flux is not significantly induced in progenitor cells treated with 4HPR even upon cytokine withdrawal.

Figure S7, related to Figure 7

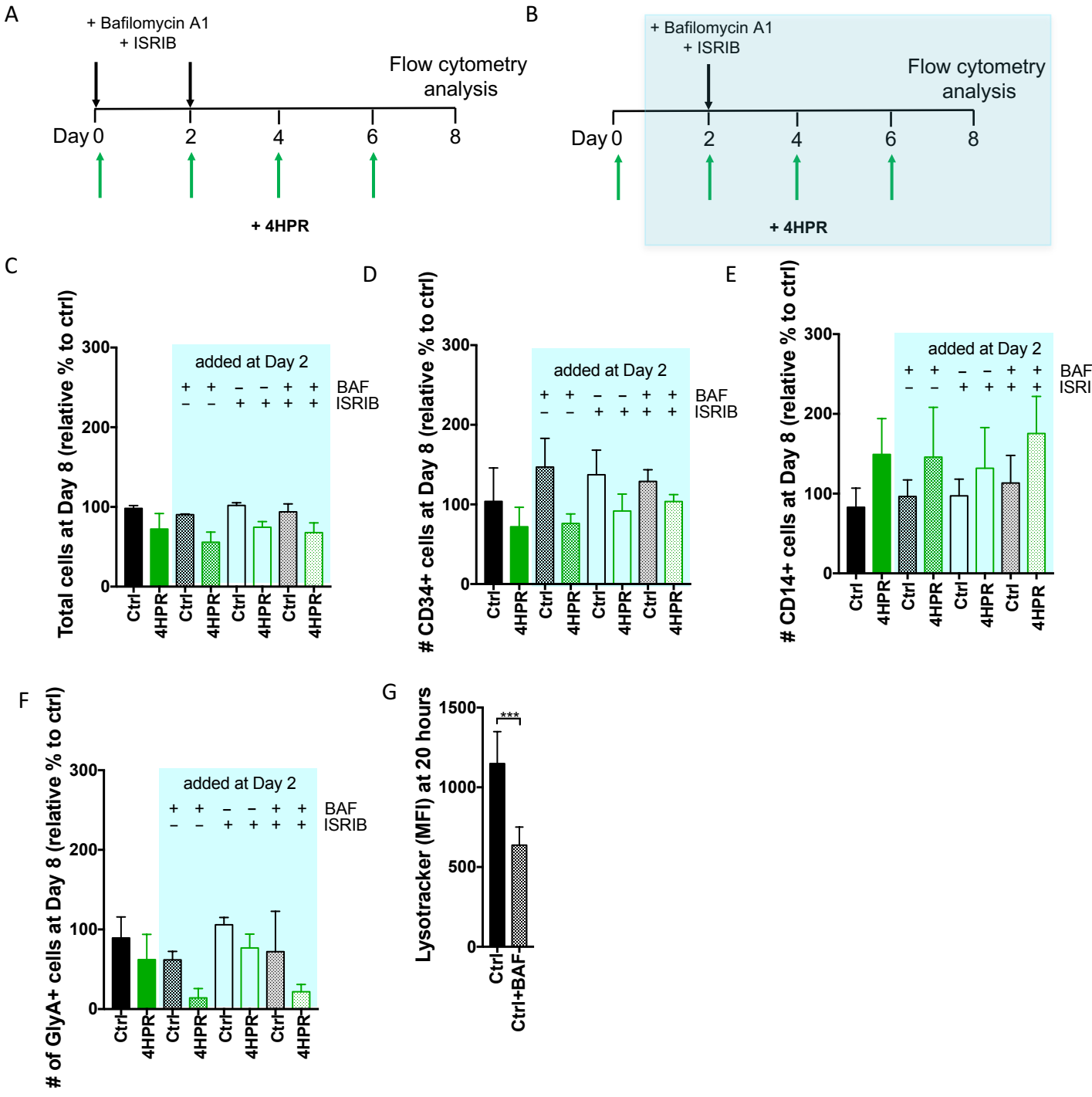

Figure S7, related to Figure 7. Sphingolipid modulation by 4HPR activates a coordinated proteostatic pro-survival response by autophagy and the Integrate Stress Response pathways. (A) Experimental scheme for Figure7A-D. (B) Experimental scheme for Figure S7C-F where BAF and ISRIB are added at day 2 only. Flow cytometry analysis at 8 days post culture for (C) total number of live cells (D) number of CD34+ cells (E) number of CD14+ cells and (F) number of GlyA+ cells represented as the relative % to ctrl treatment. (F) Lysotracker MFI was quantified by flow cytometry in DMSO control treated cells with and without BAF at 20 hours post-treatment.

Table S1, related to Figure 5 and S5. Table of GSEA pathway analysis for RNAseq data from *ex vivo* treated CB cells.

Table S2, related to Figure 5 and S5. Gene lists for selected 4HPR-altered pathways.

Table S3, related to Figure 5 and S5. Table of top 10 differentially expressed genes between Control and 4HPR treatment at day 2 for indicated pathways of Figure 5F.

Table S3

Autophagy							
gene_name	description	logFC	logCPM	LR	PValue	FDR	score
GABARAPL1	GABA type A receptor associated protein like 1	1.823	3.960	23.923	1.00E-06	1.89E-03	5.999
ANXA7	annexin A7	0.492	7.366	16.602	4.61E-05	0.037	4.336
UBC	ubiquitin C	0.677	9.738	15.045	1.05E-04	0.072	3.979
VCP	valosin containing protein	0.476	9.164	11.182	8.26E-04	0.328	3.083
SQSTM1	sequestosome 1	0.648	7.113	8.984	0.0027	0.721	2.565
RHEB	Ras homolog, mTORC1 binding	0.276	6.526	3.438	0.064	1.000	1.196
RRAGB	Ras related GTP binding B	0.325	2.785	2.587	0.108	1.000	0.968
FAM134B	NA	0.441	2.552	2.539	0.111	1.000	0.954
VPS37A	VPS37A, ESCRT-I subunit	0.254	4.867	2.500	0.114	1.000	0.944
ATG4A	autophagy related 4A cysteine peptidase	0.276	3.837	2.488	0.115	1.000	0.941
ER stress/UPR							
gene_name	description	logFC	logCPM	LR	PValue	FDR	score
PSAT1	phosphoserine aminotransferase 1	1.142	7.062	30.026	4.26E-08	1.61E-04	7.370
PSMC2	proteasome 26S subunit, ATPase 2	0.646	7.574	27.315	1.73E-07	4.35E-04	6.762
ASNS	asparagine synthetase (glutamine-hydrolyzing)	0.721	6.225	19.579	9.65E-06	0.0108	5.015
PSMC6	proteasome 26S subunit, ATPase 6	0.577	7.162	14.872	1.15E-04	0.0754	3.939
HSPA5	heat shock protein family A (Hsp70) member 5	0.458	10.488	14.327	1.54E-04	0.0918	3.814
PSMC1	proteasome 26S subunit, ATPase 1	0.623	8.108	11.212	8.13E-04	0.3279	3.090
VCP	valosin containing protein	0.476	9.164	11.182	8.26E-04	0.3279	3.083
HSP90B1	heat shock protein 90 beta family member 1	0.481	10.267	10.401	1.26E-03	0.4418	2.900
UBXN4	UBX domain protein 4	0.414	7.567	8.386	3.78E-03	0.8744	2.422
CXCL8	C-X-C motif chemokine ligand 8	2.129	5.389	7.826	5.15E-03	1.0000	2.288
Protein folding							
gene_name	description	logFC	logCPM	LR	PValue	FDR	score
UBC	ubiquitin C	0.677	9.738	15.045	1.05E-04	0.072	3.979
HSPA5	heat shock protein family A (Hsp70) member 5	0.458	10.488	14.327	1.54E-04	0.092	3.814
PSMC1	proteasome 26S subunit, ATPase 1	0.623	8.108	11.212	8.13E-04	0.328	3.090
VCP	valosin containing protein	0.476	9.164	11.182	8.26E-04	0.328	3.083
HSP90B1	heat shock protein 90 beta family member 1	0.481	10.267	10.401	1.26E-03	0.442	2.900
TTC1	tetratricopeptide repeat domain 1	0.311	6.732	4.576	0.032	1.000	1.489
BAG2	BCL2 associated athanogene 2	0.300	5.541	3.663	0.056	1.000	1.255
PFDN4	prefoldin subunit 4	0.404	5.618	2.941	0.086	1.000	1.064
EMC3	ER membrane protein complex subunit 3	0.303	5.778	2.880	0.090	1.000	1.047
ERO1LB	NA	0.376	3.472	2.878	0.090	1.000	1.047

Table S3, cont'd

Sphingolipid/Ceramide							
gene_name	description	logFC	logCPM	LR	PValue	FDR	score
B4GALNT1	beta-1,4-N-acetyl-galactosaminyltransferase 1	3.930	0.725	62.092	3.28E-15	4.94E-11	14.485
GLA	galactosidase alpha	0.444	5.912	6.158	0.013	1.000	1.883
SPTSSA	serine palmitoyltransferase small subunit A	0.152	6.162	1.454	0.228	1.000	0.642
ST3GAL5	ST3 beta-galactoside alpha-2,3-sialyltransferase 5	0.201	2.842	1.341	0.247	1.000	0.608
CLN8	CLN8, transmembrane ER and ERGIC protein	0.244	3.861	1.224	0.269	1.000	0.571
SPTLC3	serine palmitoyltransferase long chain base subunit 3	0.994	-1.547	1.216	0.270	1.000	0.568
LARGE	NA	0.504	-1.114	1.210	0.271	1.000	0.567
SGMS2	sphingomyelin synthase 2	0.321	1.240	0.906	0.341	1.000	0.467
CERS5	ceramide synthase 5	0.178	5.312	0.899	0.343	1.000	0.465
ALDH3A2	aldehyde dehydrogenase 3 family member A2	0.110	5.655	0.877	0.349	1.000	0.457
ROS							
gene_name	description	logFC	logCPM	LR	PValue	FDR	score
GCLM	glutamate-cysteine ligase modifier subunit	0.735	5.483	21.018	4.55E-06	0.007	5.342
NQO1	NAD(P)H quinone dehydrogenase 1	0.765	4.523	11.876	0.001	0.286	3.245
SRXN1	sulfiredoxin 1	0.485	5.885	7.564	0.006	1.000	2.225
GPX3	glutathione peroxidase 3	1.593	0.142	4.771	0.029	1.000	1.538
VIMP	NA	0.466	5.269	2.621	0.105	1.000	0.977
GSR	glutathione-disulfide reductase	0.295	7.268	2.528	0.112	1.000	0.951
TXN	thioredoxin	0.337	8.153	2.361	0.124	1.000	0.905
SOD1	superoxide dismutase 1	0.368	8.045	2.243	0.134	1.000	0.872
PRDX1	peroxiredoxin 1	0.293	8.920	1.625	0.202	1.000	0.694
TXNRD1	thioredoxin reductase 1	0.252	8.004	1.422	0.233	1.000	0.632
Cholesterol Biosynthesis							
gene_name	description	logFC	logCPM	LR	PValue	FDR	score
DHCR24	24-dehydrocholesterol reductase	-0.474	8.745	14.607	1.32E-04	0.083	-3.878
FASN	fatty acid synthase	-0.583	8.919	4.181	0.041	1.000	-1.389
OSBPL5	oxysterol binding protein like 5	-0.462	3.653	4.120	0.042	1.000	-1.373
LSS	lanosterol synthase	-0.431	6.553	3.092	0.079	1.000	-1.104
TM7SF2	transmembrane 7 superfamily member 2	-0.583	4.323	3.080	0.079	1.000	-1.101
CYP27B1	cytochrome P450 family 27 subfamily B member 1	-0.555	0.603	3.068	0.080	1.000	-1.098
HMGCS1	3-hydroxy-3-methylglutaryl-CoA synthase 1	-0.520	7.935	3.006	0.083	1.000	-1.081
HMGCR	3-hydroxy-3-methylglutaryl-CoA reductase	-0.363	7.682	2.823	0.093	1.000	-1.032
CRTC1	CREB regulated transcription coactivator 1	-0.340	3.368	2.603	0.107	1.000	-0.972
ELOVL6	ELOVL fatty acid elongase 6	-0.306	6.825	2.326	0.127	1.000	-0.896

Click here to access/download

Supplemental Videos and Spreadsheets

Table S1_GSEA.xlsx

Click here to access/download

Supplemental Videos and Spreadsheets

TableS2_genelists.xlsx